HOKKAIDO UNIVERSITY

Title	Dust formation and mass loss around intermediate-mass AGB stars with initial metallicity $Z_{ini} <= 10^{-4}$ in the early Universe - I. Effect of surface opacity on stellar evolution and the dust-driven wind
Author(s)	Tashibu, Shohei; Yasuda, Yuki; Kozasa, Takashi
Citation	Monthly notices of the royal astronomical society, 466(2), 1709-1732 https://doi.org/10.1093/mnras/stw3160
Issue Date	2017-04
Doc URL	http://hdl.handle.net/2115/66490
Rights	This article has been accepted for publication in Monthly notices of the royal astronomical society ©2016 The Authors Published by Oxford University Press on behalf of The Royal Astronomical Society. All rights reserved.
Type	article
File Information	MNRAS466-2 1709-1732.pdf

Instructions for use

Hokkaido University Collection of Scholarly and Academic Papers : HUSCAP

Monthly Notices of the ROYAL ASTRONOMICAL SOCIETY

MNRAS **466,** 1709–1732 (2017) doi:10.1093/mnras/stw3160

Dust formation and mass loss around intermediate-mass AGB stars with initial metallicity $Z_{\rm ini} \leq 10^{-4}$ in the early Universe – I. Effect of surface opacity on stellar evolution and the dust-driven wind

Shohei Tashibu,[1★†] Yuki Yasuda[2] and Takashi Kozasa[2,3,1★]

[1]*Department of Astronomy, University of Tokyo, 7-3-1 Hongo, Bunkyo-ku, Tokyo 113-0033, Japan*
[2]*Division of Earth and Planetary Sciences, Faculty of Science, Hokkaido University, Sapporo 060-0810, Japan*
[3]*Department of Cosmosciences, Graduate School of Science, Hokkaido University, Sapporo 060-0810, Japan*

Accepted 2016 December 2. Received 2016 December 1; in original form 2016 June 17

ABSTRACT

Dust formation and the resulting mass loss around asymptotic giant branch (AGB) stars with initial metallicity in the range $0 \leq Z_{\rm ini} \leq 10^{-4}$ and initial mass $2 \leq M_{\rm ini}/{\rm M}_{\odot} \leq 5$ are explored by hydrodynamical calculations of the dust-driven wind (DDW) along the AGB evolutionary tracks. We employ the MESA code to simulate the evolution of stars, assuming an empirical mass-loss rate in the post-main-sequence phase and considering three types of low-temperature opacity (scaled-solar, CO-enhanced and CNO-enhanced opacity) to elucidate the effect on stellar evolution and the DDW. We find that the treatment of low-temperature opacity strongly affects dust formation and the resulting DDW; in the carbon-rich AGB phase, the maximum $\dot{M}$ of $M_{\rm ini} \geq 3\ {\rm M}_{\odot}$ stars with the CO-enhanced opacity is at least one order of magnitude smaller than that with the CNO-enhanced opacity. A wide range of stellar parameters being covered, the necessary condition for driving efficient DDW with $\dot{M} \geq 10^{-6}\ {\rm M}_{\odot}\ {\rm yr}^{-1}$ is expressed as effective temperature $T_{\rm eff} \lesssim 3850$ K and $\log(\delta_{\rm C} L/\kappa_{\rm R} M) \gtrsim 10.43 \log T_{\rm eff} - 32.33$, with the carbon excess $\delta_{\rm C}$ defined as $\epsilon_{\rm C} - \epsilon_{\rm O}$, the Rosseland mean opacity $\kappa_{\rm R}$ in units of cm^2 g^{-1} in the surface layer and the stellar mass (luminosity) $M(L)$ in solar units. The fitting formulae derived for gas and dust mass-loss rates in terms of input stellar parameters could be useful for investigating the dust yield from AGB stars in the early Universe being consistent with stellar evolution calculations.

Key words: stars: abundances – stars: AGB and post-AGB – ISM: abundances – dust, extinction.

1 INTRODUCTION

While the major source of interstellar dust in the early Universe at redshift $z \gtrsim 5$ is believed to be core-collapsed supernovae (e.g. Todini & Ferrara 2001; Nozawa et al. 2003), the possibility that asymptotic giant branch (AGB) stars are an important source of dust has been suggested and investigated. Dwek, Galliano & Jones (2007) claimed that core-collapse supernovae (CCSNe) cannot reproduce the dust mass of about $4 \times 10^8\ {\rm M}_{\odot}$ in the high-redshift ($z = 6.4$) quasar J1148+5251, unless the dust mass produced is much greater than that evaluated from the observations of CCSNe in nearby galaxies or the dust destruction efficiency is much lower than that inferred from theoretical calculations. Valiante et al. (2009, 2011) have shown that AGB stars can contribute to dust enrichment even at redshifts $z < 8$–10, based on the dust yield of AGB stars with initial metallicity $Z_{\rm ini} = 10^{-3}$ calculated by Zhukovska, Gail & Trieloff (2008).

So far, investigations of dust formation around AGB stars have suggested that AGB stars with initial metallicity $Z_{\rm ini} \lesssim 10^{-3}$ cannot be assigned as the source of Si-bearing dust such as silicate, since the abundance of silicon, scaled by the initial metallicity, is so small as to prevent the formation of Si-bearing dust in the winds (Di Criscienzo et al. 2013). Thus, only carbon dust is expected to form around AGB stars with initial metallicity $Z_{\rm ini} \lesssim 10^{-3}$, owing to the progressive enrichment of carbon in the surface regions, favoured by repeated third dredge-up (TDU) events.

The upper limit on the initial mass of the star required to have production of carbon dust during the AGB phases decreases with decreasing $Z_{\rm ini}$. This is because the core mass of the star is higher when the metallicity is lower and when the core mass is above a given threshold ($\sim$0.8 ${\rm M}_{\odot}$) the stars experience hot bottom burning (HBB: Renzini & Voli 1981), with the destruction of surface carbon. Di Criscienzo et al. (2013) have inferred that only low-mass

★ E-mail: e163053c@yokohama-cu.ac.jp (ST); kozasa@sci.hokudai.ac.jp (TK)
† Present address: School of Medicine, Yokohama City University, Yokohama 236-0027, Japan.

© 2016 The Authors
Published by Oxford University Press on behalf of the Royal Astronomical Society

stars of initial mass $M_{\rm ini} \lesssim 1$ M$_\odot$ with $Z_{\rm ini} \leq 10^{-4}$ can produce carbon dust significantly and that AGB stars cannot be considered as important dust manufacturers at $Z_{\rm ini} < 10^{-4}$: this conclusion was based on their calculation for $Z_{\rm ini} = 3.0 \times 10^{-4}$ and on stellar evolution calculations with $Z_{\rm ini} \lesssim 2 \times 10^{-5}$ by Campbell & Lattanzio (2008). On the other hand, Constantino et al. (2014) confirmed that the mass threshold for HBB is different between models with and without composition-dependent low-temperature opacity. Also, even if stars experience HBB, these stars could become carbon-rich after the cease of HBB, depending on not only the treatment of low-temperature opacity but also the initial mass, as well as the mass-loss rate during evolution (e.g. Ventura & Marigo 2010; Nanni et al. 2013). Thus, the pros and cons of formation of carbon dust in AGB stars with $Z_{\rm ini} \leq 10^{-4}$ have yet to be explored by investigating how the treatment of low-temperature opacity affects the stellar evolution and dust formation.

The formation of dust and the resulting mass loss around AGB stars not only are determined by the abundances of dust-forming elements in the surface layer, but also depend sensitively on the effective temperature (see Gail & Sedlmayr 2013 and references therein). In this context, the most relevant input for stellar evolution and dust formation is the low-temperature opacity. During this last decade, it has been emphasized that the low-temperature opacity varying with the change of surface elemental composition due to TDU and HBB during the thermally pulsing AGB (TP-AGB) phase strongly affects the evolution of stars with $Z_{\rm ini} \geq 10^{-4}$ (e.g. Marigo 2002; Cristallo et al. 2007; Ventura & Marigo 2010; Constantino et al. 2014; Fishlock, Karakas & Stancliffe 2014). In particular, these authors have demonstrated that a composition-dependent low-temperature opacity makes the effective temperature decrease drastically in carbon-rich (C-rich) stars, in comparison with the scaled-solar opacity. Thus, it can be expected that the treatment of low-temperature opacity directly influences the formation of dust and the resulting dust-driven wind (DDW).

Dust formation around AGB stars is a complicated process, associated with the dynamical as well as the thermal behaviour of gas above the photosphere; dust condenses in the high-density gas induced by the shock originating from stellar pulsation, then mass loss is driven by the radiation pressure force acting on the newly formed dust (so-called pulsation-enhanced DDW: e.g. Fleischer, Gauger & Sedlmayr 1992; Winters et al. 2000). Thus, dust formation has to be treated self-consistently with the consequent gas outflow from AGB stars, considering the periodic change of stellar properties and the corresponding wind structure simultaneously. However, most previous studies on the dust yields of low-metallicity AGB stars (e.g. Ventura et al. 2012a, b, 2014; Di Criscienzo et al. 2013; Nanni et al. 2013) have followed the scheme developed by Ferrarotti & Gail (2006), without solving the formation processes of dust grains and the resulting density structure of outflowing gas self-consistently; the dust yield has been evaluated from calculations of dust growth in a stationary wind, given the number density of dust seed particles and the mass-loss rate. Thus, the derived properties of newly formed dust, such as the amount and the size, may suffer ambiguities inherent in the treatment. Although self-consistent hydrodynamical calculation of the DDW for C-rich AGB stars with subsolar metallicities has been carried out (Wachter et al. 2008), to our knowledge so far no attempt has been made for AGB stars with $Z_{\rm ini} \leq 10^{-4}$ in the early Universe.

In order to explore whether AGB stars can produce and supply carbon dust in the early Universe, first we simulate the evolution of stars with initial mass ranging from 2–5 M$_\odot$ with initial metallicity $Z_{\rm ini} \leq 10^{-4}$. In the simulations, three types of low-temperature opacity (scaled-solar, CO-enhanced and CNO-enhanced opacity) are considered, to clarify how the treatment of low-temperature opacity influences the stellar parameters related to dust formation during the AGB phase. Then, applying the calculated stellar parameters along the evolutionary track of TP-AGB to the hydrodynamical model of pulsation-enhanced DDW, we investigate the dependence of the properties of dust and the DDW produced in the TP-AGB phase on the treatment of low-temperature (surface) opacity, as well as on the initial mass and metallicity. In addition, we evaluate a necessary condition for realizing the DDW and derive the fitting formulae for gas and dust mass-loss rates caused by the DDW in terms of the input stellar parameters.

This article is organized as follows. In Section 2, we address the stellar evolution model briefly, focusing on the tools implemented in the Modules for Experiments in Stellar Astrophysics (MESA) code (Paxton et al. 2011, Paxton et al. 2013), and introduce the hydrodynamical model of pulsation-enhanced DDW used in this study. Section 3 provides the results of stellar evolution calculations and shows how the stellar parameters (e.g. effective temperature and elemental composition in the surface layer) controlling the dust formation and mass loss during the TP-AGB phase are affected by the treatment of low-temperature opacity. Then, the dependence of the dust formation and resulting mass loss during the C-rich AGB phase on the low-temperature opacity, as well as on the initial mass and metallicity, is presented in Section 4. In Section 5, a necessary condition for producing an efficient DDW with mass-loss rate $\dot{M} \geq 10^{-6}$ M$_\odot$ yr^{-1} and formulae for the gas and dust mass-loss rates are derived, and the implication on the evolution of AGB stars and dust formation in the early Universe is discussed. A summary is presented in Section 6. The input stellar parameters of the hydrodynamical calculations, as well as the derived properties of the DDW with $\dot{M} \geq 10^{-7}$ M$_\odot$ yr^{-1}, are tabulated for models with CO-enhanced and CNO-enhanced opacities in Appendix A.

2 THE MODELS

The formation of carbon dust and the resulting mass loss around AGB stars with $Z_{\rm ini} \leq 10^{-4}$ after the C-rich star stage is reached are investigated through two separate steps: first, given the initial mass and metallicity, the stellar evolution is simulated from the pre-main-sequence to the end of the AGB phase. Secondly, the stellar parameters roughly every 0.05 M$_\odot$ along the evolutionary track on TP-AGB are applied to the hydrodynamical model of a pulsation-enhanced DDW to evaluate the formation of carbon dust and the resulting DDW in the C-rich AGB phase. Here, we describe briefly the models used in these two steps.

2.1 Stellar evolution

We employ the MESA code for the calculation of stellar evolution models, evolved from the pre-main-sequence up to the end of the AGB phase of stars with initial masses $M_{\rm ini} = 2, 3, 4$ and 5 M$_\odot$ and metallicities $Z_{\rm ini} = 0, 10^{-7}, 10^{-6}, 10^{-5}$ and 10^{-4}. In addition to the treatment of convection, we describe the low-temperature opacities and the mass-loss formula implemented in the MESA code for the purpose of the present study in the following subsections.

2.1.1 Convection

In the calculations, the standard mixing-length theory (MLT: Cox & Giuli 1968) is applied to treat convection as a diffusive process within convective regions, defined according to the

Schwarzschild criterion, $\nabla_{\rm ad} < \nabla_{\rm rad}$, where $\nabla_{\rm ad}$ and $\nabla_{\rm rad}$ are the adiabatic and radiative temperature gradient, respectively. In the convective region involving nuclear burning, MESA solves the coupled structure, burning and mixing equations, as detailed in Paxton et al. (2011, Paxton et al. 2013). The mixing-length parameter $\alpha_{\rm MLT}$ is set to be 2.0 as a standard value to reproduce the evolution of the Sun. Overshooting expresses the physical concept of an exponentially decaying velocity field beyond the convective boundary and overshoot mixing is treated as a time-dependent, diffusive process, with the overshoot-mixing diffusion coefficient defined as $D_{\rm OV} = D_{\rm conv,0} \exp(-2z/fH_{\rm P})$, where $D_{\rm conv,\,0}$ is the MLT diffusion coefficient at the boundary, z is the distance from the boundary, f is a free parameter called the overshooting parameter and $H_{\rm P}$ is the pressure scaleheight (Herwig 2000). For overshooting parameters, we adopt $f = 0.014$ at all convective boundaries, except for the bottom of the He-shell flash region, at which f is set to be 0.008 throughout the evolution after the first thermal pulse (TP), referring to Paxton et al. (2011); note that we adpot $f = 0.014$ at the bottom of the convective envelope, instead of $f = 0.126$, since we consider that the formation of a ^{13}C pocket is not relevant to the purpose of this article. We note that the MLT scheme leads to less efficient HBB than the full spectrum of turbulence (FST) scheme (Canuto & Mazzitelli 1991), as discussed by Ventura & D'Antona (2005). Thus, if the FST scheme were applied, less carbon dust would be formed, since carbon burning by HBB would be much stronger.

2.1.2 *Low-temperature opacity*

In order to clarify the role played by low-temperature opacities, not only regarding stellar evolution but also in the formation of carbon dust and resulting mass loss during the AGB phase, in the MESA code we implement three types of low-temperature opacity: (1) the scaled-solar opacity, with the elemental composition of metals scaled by the solar composition (Grevesse & Noels 1993) according to the initial metallicity; (2) the CO-enhanced opacity, in which the opacity is calculated according to the enhancement of C and O abundances with respect to the scaled-solar values; (3) the CNO-enhanced opacity, which also includes the variation of N with respect to the scaled-solar value, besides the variation of C and O abundances. Since the CN molecule dominates the Rosseland mean opacity at low temperature, $\log T \lesssim 3.6$ (Marigo & Aringer 2009), the CNO-enhanced opacity is, among the three possibilities, the most suitable one to describe the evolution of AGB stars.

The opacity tables are constructed using the ÆSOPUS tool (Marigo & Aringer 2009) and are incorporated into the MESA code; the tables consist of five grids of metallicity ($Z = 10^{-12}$, 10^{-7}, 10^{-6}, 10^{-5} and 10^{-4}), three grids of the mass fraction of hydrogen ($X_{\rm H} = 0.50$, 0.65 and 0.80) and 16 grids of the increment of the mass fraction ($0 \leq {\rm d}X_i \leq 9.72 \times 10^{-2}$) for element i ($i =$ C, N and O). The grids of temperature T (in units of K) and the parameter $R = \rho/(T/10^6)^3$, with gas density ρ in c.g.s. units, cover the ranges $3.20 \leq \log T \leq 4.50$ and $-8.0 \leq \log R \leq 1.0$, respectively. Note that we adopt the opacity tables for $Z = 10^{-12}$ as representative of $Z = 0$. For the high-temperature opacity ($\log T \geq 4.0$), we adopt the Opacity Project at Livermore (OPAL) type 2 opacities (Iglesias & Rogers 1993, 1996) implemented in the MESA code, accounting for the enhancement of carbon and oxygen during the evolution. The opacity in the range $3.8 \leq \log T \leq 4.0$ is calculated by interpolating linearly between the low- and high-temperature opacity tables at a fixed $\log R$.

2.1.3 *Mass loss*

Mass loss during the evolution of low- and intermediate-mass stars plays a decisive role in determining the efficiency of TDU and HBB (e.g. Weiss & Ferguson 2009). In previous studies, empirical and/or theoretical mass-loss formulae have been applied: for example, Weiss & Ferguson (2009) applied the Reimers formula (Reimers 1975) on the red giant branch (RGB) and the AGB with pulsation periods $P \leq 400$ d and then the formulae proposed by van Loon et al. (2005) for oxygen-rich (O-rich) AGB and Wachter et al. (2002) for C-rich AGB; the formulae by Vassiliadis & Wood (1993) and Blöcker (1995) were adopted for the whole AGB phase in Ferrarotti & Gail (2006) and Ventura et al. (2012a,b), respectively. Although the DDW mechanism has been believed to be plausible for C-rich AGB stars in galaxies with solar and subsolar metallicities at the present time, we have no convincing knowledge of whether intermediate-mass stars in the early Universe, with $Z_{\rm ini} \leq 10^{-4}$, can form carbon dust efficiently enough to drive mass loss on the AGB.

The aim of this article is to reveal whether and in what conditions the formation of carbon dust and the consequent DDW onset on the AGB, as the first step to exploring the role of AGB stars as the source of dust in the early Universe. Thus, we apply an empirical mass-loss formula in the post-main-sequence phase for simplicity. In this article, we adopt the formula by Schröder & Cuntz (2005, hereinafter SC05), since the formula reproduces the mass-loss rate on the RGB reasonably; although the recent population synthesis model of AGB stars in metal-poor galaxies prefers a modified SC05 as the mass-loss formula on the AGB before the onset of DDW, its application on the RGB is questionable (Rosenfield et al. 2014). The formula of SC05 is given by

$$\dot{M}_{\rm SC05} = \eta \frac{LR}{M} \left(\frac{T_{\rm eff}}{4000\,{\rm K}}\right)^{3.5} \left(1 + \frac{1}{4300g}\right), \tag{1}$$

where the mass-loss rate is in units of $\rm M_{\odot}\ yr^{-1}$, the effective temperature $T_{\rm eff}$ is in units of K and the stellar mass M, luminosity L and surface gravity g are in solar units. In the calculations, we adopt the fitting parameter $\eta = 8 \times 10^{-14}$; the value of η is adjusted by fitting to the observed mass-loss rates of red giant stars in globular clusters with different metallicities (SC05), with which the formula reproduces the observed mass-loss rates of Galactic giants and supergiants well (Schröder & Cuntz 2007).

2.2 Dust-driven wind

Here, we describe the hydrodynamical model of a pulsation-enhanced DDW by Yasuda & Kozasa (2012) employed in this article. The hydrodynamical model treats the nucleation and growth processes of carbon dust in the gas lifted up by the pulsation shock and the consequent DDW self-consistently. The model adopts the scheme for the formation of carbon grains proposed by Gauger, Gail & Sedlmayr (1990) and includes the decay process of dust by heating due to backward radiation. Given the stellar parameters at the photosphere (see below) at a given epoch during the AGB phase, the model allows evaluation of the physical quantities related to dust formation: the time evolution of the mass-loss rate, gas velocity and condensation efficiency of carbon dust (defined as the ratio of carbon locked into dust to carbon available for dust formation), as well as the amount and size distribution of dust particles in the wind, together with their time-averaged values at the outer boundary of the hydrodynamical model.

The stellar parameters necessary for hydrodynamical model calculations are the current stellar mass M, luminosity L, effective temperature $T_{\rm eff}$, abundances of H, He, C, N and O, Rosseland mean opacity $\kappa_{\rm R}$ in the photosphere, period P_0 and velocity amplitude $\Delta u_{\rm p}$ of pulsation. The temporal evolution of the stellar parameters, except for the period and amplitude of pulsation, can be obtained from the stellar evolution calculation. For the pulsation period, we apply the formula for the fundamental radial mode of pulsation by Ostlie & Cox (1986), which is given by

$$\log P_0 = -1.92 - 0.73 \log M + 1.86 \log R, \qquad (2)$$

where P_0 is in units of days and the stellar mass M and stellar radius R are in solar units. As for the velocity amplitude of pulsation, little is known, as mentioned in Gail & Sedlmayr (2013), though Wood (1986) have estimated it to be a few km s^{-1}, by adjusting the variable pressure at the inner boundary to a certain photospheric density deduced from observations. Thus, in this article, $\Delta u_{\rm p}$ is set to be 2 km s^{-1} as a reference value. We address the reader to Yasuda & Kozasa (2012) for details of the numerical schemes for the formation process of carbon grains and the dust-driven wind.

In the calculations, we use the optical constants of astronomical graphite (Draine 1985) for carbon dust. The physical quantities characterizing the dust formation and resulting DDW presented in the following sections are specified by the values averaged over the final 60 pulsation cycles at the outer boundary placed at 25 times the initial stellar radius of the hydrodynamical model. Note that we avoid calculations at the current stellar mass in the short time intervals of TPs during the evolution, since convergence problems often occur just after the onset of TP in the stellar evolution calculations, as presented in the following subsection.

2.3 Convergence problem

During the stellar evolution calculation, we often come across convergence problems just after the onset of TP, when the effective temperature decreases down to ∼3200 K. The failed convergency is not caused by the dominance of radiation pressure in the convective envelope, i.e. the small ratio of gas pressure to total pressure, β, but may be associated with the opacity, as argued by Karakas & Lattanzio (2007). While investigation of the precise cause of the convergence problems is postponed to a future work, in the present calculations we avoid convergence difficulties as follows: we set a minimum temperature ($T_{\rm min,op}$) from just before the onset of TP to the beginning of TDU and the low-temperature opacity is replaced with that calculated using $T_{\rm min,op}$ in a region where the local temperature is lower than $T_{\rm min,op}$.

This method might affect the TDU efficiency parameter λ, defined as the ratio between the mass dredged up after a thermal pulse, $\Delta M_{\rm DUP}$, and the increment of core mass during the preceding interpulse phase, $\Delta M_{\rm c}$ (e.g. Herwig 2005); in the calculations of model stars with CNO-enhanced opacity, for example, the largest difference of λ between successive TDUs with and without the convergence problem is 0.24 for $M_{\rm ini} = 5$ M$_\odot$, with $Z_{\rm ini} = 10^{-4}$. Such a degree of difference can be seen between successive TDUs with no convergence problem. By setting the different values of $\log T_{\rm min,op}$ for the successive TDUs at $M = 1.69$ M$_\odot$ and 1.60 M$_\odot$ during the evolution of $M_{\rm ini} = 3$ M$_\odot$ with $Z_{\rm ini} = 10^{-7}$, the largest difference of λ reaches 0.404. However, only two models ($M_{\rm ini} = 3$ M$_\odot$ with $Z_{\rm ini} = 10^{-7}$ and $M_{\rm ini} = 4$ M$_\odot$ with $Z_{\rm ini} = 0$) suffer such a large increment at a TDU among the last few TDUs before the evolution calculation finally stops. In addition, the effective temperature quickly changes in a short time interval of TP. Thus, we consider that the prescription for dealing with the convergence problem cannot cause a serious issue against the aim of this article.

3 EVOLUTION OF LOW-METALLICITY AGB STARS

Table 1 summarizes the stellar models and the calculated quantities characterizing their TP-AGB phase: initial metallicity $Z_{\rm ini}$; type of low-temperature opacity; final stellar (core) mass $M_{\rm tot,f}$ ($M_{\rm c,f}$); total number of TPs; total number of TDUs; threshold stellar mass $M_{\rm C/O>1}$, defined as the mass of the star at the time after which the C/O ratio in the surface layers keeps exceeding unity; maximum temperature at the bottom of the convective envelope during the TP-AGB phase $T_{\rm bce,max}$; minimum effective temperature during the interpulse phases $T_{\rm eff,min}$; final carbon excess (defined as $\delta_{\rm C} \equiv \epsilon_{\rm C} - \epsilon_{\rm O}$ with $\epsilon_{\rm C}$ ($\epsilon_{\rm O}$) the abundance of C (O) by number relative to H); and also the final mass fractions of C, N and O in the surface layer. Note that 'final' does not always mean the end of the AGB phase. The models that fail to evolve to the end of the TP-AGB phase due to convergence problems are denoted by the superscript *f*. Also, models undergoing HBB (weak HBB) during evolution are specified by the superscript H (WH) attached to the value of $T_{\rm bce,max}$.

How the difference in the treatment of low-temperature opacity affects the evolution and structure of low-metallicity stars has been analysed in the work by Constantino et al. (2014), aimed at clarifying whether use of composition-dependent low-temperature opacities is necessary for modelling the evolution of metal-poor AGB stars. Here, we briefly address the effects of the treatment of low-temperature opacity on the evolution of AGB stars in relation to dust formation, primarily referring to the result of calculations for $Z_{\rm ini} = 10^{-7}$. In the C-rich envelope, the contribution of C_2 and CN molecules to the opacity is enhanced around $T = 3500$ K (see fig. 13 in Marigo & Aringer 2009). Thus, for a given set of gas density and temperature, the value of low-temperature opacity increases in the order scaled-solar, CO-enhanced and finally CNO-enhanced. In what follows, a model star with scaled-solar (CO-enhanced, CNO-enhanced) opacity is referred to as the scaled-solar (CO-enhanced, CNO-enhanced) model.

3.1 CNO abundances and carbon excess $\delta_{\rm C}$ in the surface layer

Fig. 1 shows the effects of the treatment of low-temperature opacity on the evolution of the mass fractions of C, N and O (left panel) and the carbon excess $\delta_{\rm C}$ and the C/O ratio (right panel) in the surface regions of stars with $M_{\rm ini} = 2$ (top), 3 (middle) and 4 M$_\odot$ (bottom) with $Z_{\rm ini} = 10^{-7}$.

The star with $M_{\rm ini} = 2$ M$_\odot$ and $Z_{\rm ini} = 10^{-7}$ becomes C-rich after the first TDU and the final carbon excess $\delta_{\rm C}$ exceeds 0.001, regardless of the treatment of low-temperature opacity. This holds for all the 2-M$_\odot$ models with $Z_{\rm ini} \leq 10^{-4}$ (see Table 1). $\delta_{\rm C}$ and the surface mass fractions of C and O increase with time and become larger in decreasing order of the values of the low-temperature opacities. On the other hand, without HBB the surface mass fraction of N during the TP-AGB phase is not affected by the treatment of low-temperature opacities. Also, the C/O ratio declines quickly after first TDU and then converges to a constant, larger than 10, almost independent of the type of low-temperature opacity.

The 4-M$_\odot$ models with $Z_{\rm ini} = 10^{-7}$, regardless of the treatment of low-temperature opacity, undergo HBB after several TDU events (see the bottom left panel of Fig. 1). While $\delta_{\rm C}$ increases with time during the initial AGB phases following the first TDU, the mass fraction of N (C) in the surface regions increases (decreases) quickly

Table 1. Models and characteristic quantities during AGB phase: initial metallicity $Z_{\rm ini}$, type of low-temperature opacity ($\kappa_{\rm solar}$, $\kappa_{\rm CO}$ and $\kappa_{\rm CNO}$ denote scaled-solar, CO-enhanced and CNO-enhanced opacities, respectively), final stellar mass $M_{\rm tot,f}$ in solar units, final core mass $M_{\rm c,f}$ in solar units with the superscript '*f*' for those models that fail to evolve to the end of AGB phase, total number of TPs $N_{\rm TP}$, total number of TDUs $N_{\rm TDU}$, stellar mass below which C/O > 1 $M_{\rm C/O>1}$ in solar units, maximum temperature at the bottom of convective envelope during interpulse phases $T_{\rm bce,max}$ in units of 10^6 K with the superscript H (WH) for the models that experience HBB (weak HBB), minimum effective temperature during interpulse phases $T_{\rm eff,min}$ in units of K, final carbon excess $\delta_{\rm c,f} \times 10^4$ and the mass fractions of C, N and O in the surface layer $X_{\rm f}$(C), $X_{\rm f}$(N) and $X_{\rm f}$(O), respectively. Note that the models of $M_{\rm ini} = 5$ M$_{\odot}$ with $Z_{\rm ini} = 0$ and 10^{-7} are excluded, since the star does not form carbon dust without undergoing TDU on TP-AGB.

$Z_{\rm ini}$	κ	$M_{\rm tot,f}$	$M_{\rm c,f}$	$N_{\rm TP}$	$N_{\rm TDU}$	$M_{\rm C/O>1}$	$T_{\rm bce,max}$	$T_{\rm eff,min}$	$\delta_{\rm c,f} \times 10^4$	$X_{\rm f}$(C)	$X_{\rm f}$(N)	$X_{\rm f}$(O)
$M_{\rm ini} = 2.0$M$_{\odot}$												
10^{-4}	$\kappa_{\rm solar}$	0.695	0.695	20	19	1.88	10.0	3927	49.4	4.20×10^{-2}	1.68×10^{-4}	4.74×10^{-3}
10^{-4}	$\kappa_{\rm CO}$	0.692	0.692	17	16	1.88	7.24	3254	22.0	2.02×10^{-2}	5.22×10^{-5}	2.29×10^{-3}
10^{-4}	$\kappa_{\rm CNO}$	0.690^{f}	0.690	17	16	1.88	6.92	3136	25.5	2.32×10^{-2}	5.97×10^{-5}	2.63×10^{-3}
10^{-5}	$\kappa_{\rm solar}$	0.698	0.698	17	16	1.84	10.0	3974	35.8	3.12×10^{-2}	3.47×10^{-4}	3.28×10^{-3}
10^{-5}	$\kappa_{\rm CO}$	0.695	0.695	15	14	1.84	7.60	3439	24.1	2.16×10^{-2}	3.15×10^{-4}	2.21×10^{-3}
10^{-5}	$\kappa_{\rm CNO}$	0.689^{f}	0.689	13	12	1.84	6.04	2939	22.0	2.00×10^{-2}	2.94×10^{-4}	2.09×10^{-3}
10^{-6}	$\kappa_{\rm solar}$	0.707	0.707	17	17	1.83	10.0	3980	25.7	2.25×10^{-2}	3.59×10^{-4}	2.27×10^{-3}
10^{-6}	$\kappa_{\rm CO}$	0.703	0.703	16	16	1.83	8.07	3575	20.2	1.79×10^{-2}	3.96×10^{-4}	3.02×10^{-3}
10^{-6}	$\kappa_{\rm CNO}$	0.699^{f}	0.699	14	14	1.83	6.17	3059	14.5	1.31×10^{-2}	3.26×10^{-4}	1.33×10^{-3}
10^{-7}	$\kappa_{\rm solar}$	0.712	0.712	20	18	1.81	10.4	3984	23.5	2.04×10^{-2}	2.08×10^{-4}	2.11×10^{-3}
10^{-7}	$\kappa_{\rm CO}$	0.711	0.711	17	16	1.81	8.45	3627	18.8	1.65×10^{-2}	2.11×10^{-4}	1.72×10^{-3}
10^{-7}	$\kappa_{\rm CNO}$	0.707^{f}	0.707	17	14	1.81	6.79	3153	15.0	1.34×10^{-2}	1.98×10^{-4}	1.42×10^{-3}
0	$\kappa_{\rm solar}$	0.727	0.727	26	16	1.76	10.7	3990	21.4	1.79×10^{-2}	2.70×10^{-4}	1.72×10^{-3}
0	$\kappa_{\rm CO}$	0.726	0.726	25	14	1.76	9.02	3695	14.5	1.24×10^{-2}	2.23×10^{-4}	1.18×10^{-3}
0	$\kappa_{\rm CNO}$	0.723	0.723	23	13	1.76	7.43	3272	12.6	1.08×10^{-2}	2.21×10^{-4}	1.03×10^{-3}
$M_{\rm ini} = 3.0$M$_{\odot}$												
10^{-4}	$\kappa_{\rm solar}$	0.823	0.823	29	27	1.64	$74.8^{\rm H}$	3912	16.1	1.56×10^{-2}	1.84×10^{-2}	4.05×10^{-3}
10^{-4}	$\kappa_{\rm CO}$	0.828	0.827	29	27	1.67	$74.3^{\rm H}$	3521	13.7	1.35×10^{-2}	1.75×10^{-2}	3.50×10^{-3}
10^{-4}	$\kappa_{\rm CNO}$	1.121^{f}	0.828	28	26	2.75	$56.9^{\rm WH}$	2693	21.6	1.95×10^{-2}	1.49×10^{-3}	2.20×10^{-3}
10^{-5}	$\kappa_{\rm solar}$	0.820	0.819	28	26	1.56	$73.6^{\rm H}$	3960	19.9	1.87×10^{-2}	1.90×10^{-2}	4.44×10^{-3}
10^{-5}	$\kappa_{\rm CO}$	0.868^{f}	0.818	29	26	1.58	$73.2^{\rm H}$	3660	13.1	1.31×10^{-2}	1.82×10^{-2}	3.65×10^{-3}
10^{-5}	$\kappa_{\rm CNO}$	1.122^{f}	0.822	26	24	2.68	$56.0^{\rm WH}$	2698	22.0	1.97×10^{-2}	9.89×10^{-4}	2.09×10^{-3}
10^{-6}	$\kappa_{\rm solar}$	0.815	0.815	28	26	1.66	$72.2^{\rm H}$	3969	19.3	1.78×10^{-2}	1.87×10^{-2}	4.15×10^{-3}
10^{-6}	$\kappa_{\rm CO}$	0.817	0.817	28	26	1.70	$71.7^{\rm H}$	3685	17.5	1.62×10^{-2}	1.77×10^{-2}	3.61×10^{-3}
10^{-6}	$\kappa_{\rm CNO}$	1.510^{f}	0.820	24	22	2.60	$53.9^{\rm WH}$	2873	18.2	1.61×10^{-2}	5.62×10^{-4}	1.47×10^{-3}
10^{-7}	$\kappa_{\rm solar}$	0.816	0.816	28	27	1.66	$71.5^{\rm H}$	3980	22.4	1.93×10^{-2}	1.90×10^{-2}	3.86×10^{-3}
10^{-7}	$\kappa_{\rm CO}$	0.820	0.819	28	27	1.79	$71.1^{\rm H}$	3726	18.4	1.61×10^{-2}	1.80×10^{-2}	3.21×10^{-3}
10^{-7}	$\kappa_{\rm CNO}$	1.072^{f}	0.828	27	26	2.57	$47.8^{\rm WH}$	2883	22.3	1.88×10^{-2}	3.55×10^{-4}	1.77×10^{-3}
0	$\kappa_{\rm solar}$	0.805	0.805	40	37	2.55	$61.0^{\rm WH}$	4011	16.2	1.30×10^{-2}	1.49×10^{-2}	2.35×10^{-3}
0	$\kappa_{\rm CO}$	0.807	0.807	40	37	2.55	$50.3^{\rm WH}$	3543	27.0	2.04×10^{-2}	7.72×10^{-4}	1.88×10^{-3}
0	$\kappa_{\rm CNO}$	1.195^{f}	0.798	32	31	2.55	31.9	2997	21.2	1.62×10^{-2}	3.75×10^{-4}	1.55×10^{-3}
$M_{\rm ini} = 4.0$M$_{\odot}$												
10^{-4}	$\kappa_{\rm solar}$	0.914^{f}	0.880	36	34	1.50	$87.7^{\rm H}$	3928	13.5	1.17×10^{-2}	1.71×10^{-2}	2.73×10^{-3}
10^{-4}	$\kappa_{\rm CO}$	0.968^{f}	0.882	36	34	1.57	$87.7^{\rm H}$	3659	10.4	9.31×10^{-3}	1.67×10^{-2}	2.38×10^{-3}
10^{-4}	$\kappa_{\rm CNO}$	1.237^{f}	0.882	36	35	1.90	$87.0^{\rm H}$	2868	7.62	7.04×10^{-3}	1.41×10^{-2}	1.83×10^{-3}
10^{-5}	$\kappa_{\rm solar}$	0.878	0.878	36	33	1.56	$87.0^{\rm H}$	3968	15.4	1.30×10^{-2}	1.68×10^{-2}	2.66×10^{-3}
10^{-5}	$\kappa_{\rm CO}$	0.918^{f}	0.878	36	33	1.64	$86.9^{\rm H}$	3768	11.9	1.04×10^{-2}	1.65×10^{-2}	2.31×10^{-3}
10^{-5}	$\kappa_{\rm CNO}$	1.270^{f}	0.878	35	33	1.92	$86.2^{\rm H}$	2915	6.75	6.31×10^{-3}	1.42×10^{-2}	1.70×10^{-3}
10^{-6}	$\kappa_{\rm solar}$	0.862	0.861	36	33	1.59	$84.3^{\rm H}$	3975	16.4	1.37×10^{-2}	1.77×10^{-2}	2.68×10^{-3}
10^{-6}	$\kappa_{\rm CO}$	0.862	0.862	36	33	1.62	$84.2^{\rm H}$	3774	15.0	1.26×10^{-2}	1.72×10^{-2}	2.46×10^{-3}
10^{-6}	$\kappa_{\rm CNO}$	1.236^{f}	0.859	35	33	1.94	$83.3^{\rm H}$	2882	7.42	6.89×10^{-3}	1.53×10^{-2}	1.81×10^{-3}
10^{-7}	$\kappa_{\rm solar}$	0.858	0.857	37	32	1.57	$83.5^{\rm H}$	3982	16.4	1.35×10^{-2}	1.80×10^{-2}	2.68×10^{-3}
10^{-7}	$\kappa_{\rm CO}$	0.893^{f}	0.857	37	32	1.62	$83.4^{\rm H}$	3785	13.0	1.09×10^{-2}	1.73×10^{-2}	2.24×10^{-3}
10^{-7}	$\kappa_{\rm CNO}$	1.196^{f}	0.855	35	33	1.98	$82.5^{\rm H}$	2860	8.50	7.64×10^{-3}	1.52×10^{-2}	1.92×10^{-3}
0	$\kappa_{\rm solar}$	0.832	0.832	44	41	1.64	$79.4^{\rm H}$	4019	9.16	7.77×10^{-3}	2.26×10^{-2}	2.52×10^{-3}
0	$\kappa_{\rm CO}$	0.833	0.833	45	41	1.64	$79.2^{\rm H}$	3834	8.79	7.46×10^{-3}	2.23×10^{-2}	2.40×10^{-3}
0	$\kappa_{\rm CNO}$	1.193^{f}	0.835	44	41	2.12	$77.9^{\rm H}$	2867	8.43	7.04×10^{-3}	1.80×10^{-2}	1.96×10^{-3}
$M_{\rm ini} = 5.0$M$_{\odot}$												
10^{-4}	$\kappa_{\rm solar}$	1.133^{f}	0.969	44	41	1.53	$101^{\rm H}$	3984	6.59	6.55×10^{-3}	1.59×10^{-2}	2.58×10^{-3}
10^{-4}	$\kappa_{\rm CO}$	1.066^{f}	0.971	45	36	1.59	$100^{\rm H}$	3777	7.88	7.48×10^{-3}	1.53×10^{-2}	2.64×10^{-3}
10^{-4}	$\kappa_{\rm CNO}$	1.329^{f}	0.968	44	41	1.73	$100^{\rm H}$	3096	4.49	4.96×10^{-3}	1.43×10^{-2}	2.35×10^{-3}
10^{-5}	$\kappa_{\rm solar}$	1.054^{f}	0.947	42	37	1.51	$98.2^{\rm H}$	3985	9.15	8.31×10^{-3}	1.63×10^{-2}	2.64×10^{-3}
10^{-5}	$\kappa_{\rm CO}$	1.019^{f}	0.947	42	38	1.56	$97.9^{\rm H}$	3837	10.0	8.97×10^{-3}	1.62×10^{-2}	2.76×10^{-3}
10^{-5}	$\kappa_{\rm CNO}$	1.242^{f}	0.945	42	38	1.77	$97.5^{\rm H}$	3073	5.65	5.77×10^{-3}	1.50×10^{-2}	2.40×10^{-3}
10^{-6}	$\kappa_{\rm solar}$	1.040^{f}	0.941	44	35	1.51	$98.2^{\rm H}$	3985	9.60	8.63×10^{-3}	1.62×10^{-2}	2.60×10^{-3}
10^{-6}	$\kappa_{\rm CO}$	0.994^{f}	0.942	45	36	1.56	$98.3^{\rm H}$	3849	11.0	9.61×10^{-3}	1.59×10^{-2}	2.67×10^{-3}
10^{-6}	$\kappa_{\rm CNO}$	1.317^{f}	0.941	44	35	1.77	$98.0^{\rm H}$	3076	4.97	5.25×10^{-3}	1.48×10^{-2}	2.22×10^{-3}

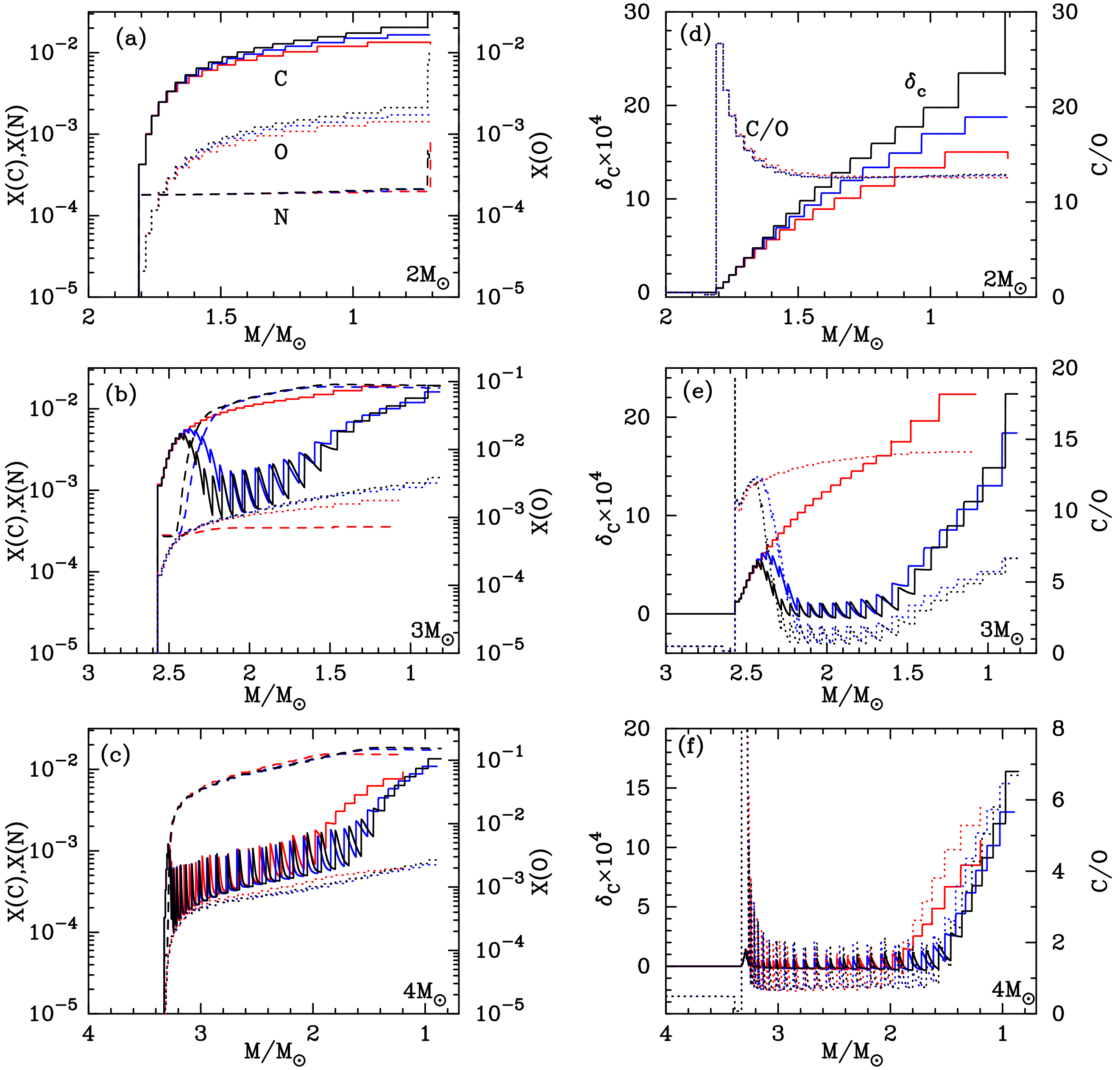

Figure 1. The effect of low-temperature opacity on the temporal evolution of mass fractions of C, N and O (left panel) and carbon excess δ_C and C/O ratio (right panel) in the surface layer for $M_{ini} = 2$ (top), 3 (middle) and 4 $M_\odot$ (bottom) stars with $Z_{ini} = 10^{-7}$. The scaled-solar, CO-enhanced and CNO-enhanced models are coloured in black, blue, and red, respectively. The mass fraction of C (N, O) is denoted by the solid (dashed, dotted) line in the left panel and δ_C (C/O ratio) by the solid (dotted) line in the right panel.

after the onset of HBB. Thus, the combination of TDU and HBB makes the elemental composition in the surface regions C-rich and O-rich alternately. However, HBB ceases after the stellar mass reduces to 1.57, 1.62 and 1.98 $M_\odot$ for the scaled-solar, CO-enhanced and CNO-enhanced models, respectively. Consequently, the subsequent TDUs cause the stars to be C-rich again and δ_C as well as the C/O ratio to increase monotonically with time. The carbon excess δ_C in the surface region is more enhanced in the CNO-enhanced model with the largest threshold mass $M_{C/O>1}$ than in other opacity models at the same current stellar mass. Although the details depend on the initial metallicity, this behaviour holds for all the 4-$M_\odot$ models with $Z_{ini} \leq 10^{-4}$ and the 5-$M_\odot$ models with $Z_{ini} \geq 10^{-6}$; TDU is not experienced during the TP-AGB phase in the models with $M_{ini} = 5\,M_\odot$ with $Z_{ini} = 0$ and 10^{-7}, thus both models are excluded from Table 1 and the following discussion.

The evolution of the 3-$M_\odot$ model with $Z_{ini} = 10^{-7}$ is sensitive to the treatment of low-temperature opacity. The CNO-enhanced model is always C-rich in the TP-AGB phase, with very weak HBB in the early phase. On the other hand, the scaled-solar and CO-enhanced models experience stronger HBB until the stellar masses are reduced to 1.66 and 1.77 $M_\odot$, respectively, and then turn out to be C-rich. These behaviours are common to all the $M_{ini} = 3\,M_\odot$ models with $Z_{ini} \geq 10^{-7}$; the $M_{ini} = 3\,M_\odot$ models with $Z_{ini} = 0$ are always C-rich in their TP-AGB phases, since the scaled-solar, CO-enhanced and CNO-enhanced models experience weak, very weak and no HBB, respectively, as shown in Fig. 2.

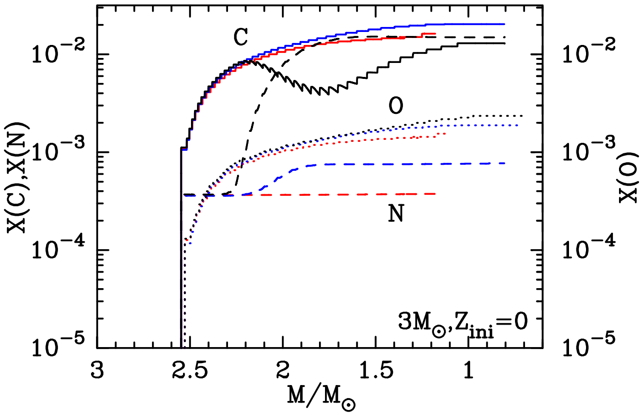

Figure 2. Same as the left panel of Fig. 1, but for $M_{\rm ini}$ = 3 M$_{\odot}$ with $Z_{\rm ini} = 0$.

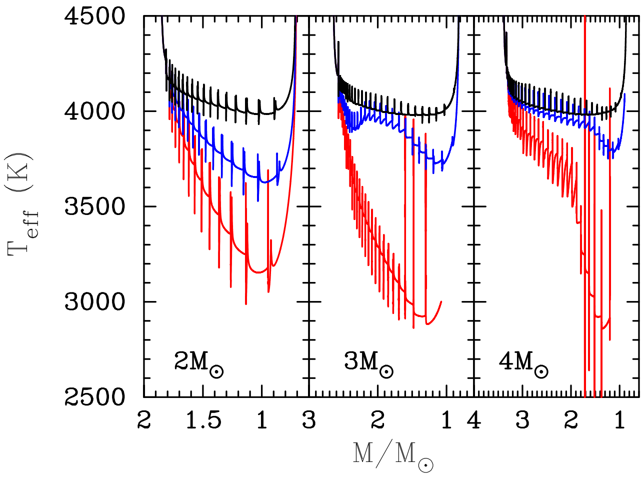

Figure 3. The effect of the low-temperature opacity on the time evolution of effective temperature for the same models with $Z_{\rm ini} = 10^{-7}$ in Fig. 1; $M_{\rm ini} = 2$ (left), 3 (middle), and 4 M$_{\odot}$ (right) models with scaled-solar (black line), CO-enhanced (blue line) and CNO-enhanced (red line) opacities.

We note that, in the case of $M_{\rm ini} = 3$ M$_{\odot}$, the value of $M_{\rm C/O>1}$ is significantly larger in the CNO-enhanced model than in the other two models. Thus, it can be expected that the model of $M_{\rm ini} = 3$ M$_{\odot}$ with the CNO-enhanced opacity could start to form carbon dust at a significantly larger stellar mass. In addition, it should be emphasized that the carbon excess $\delta_{\rm C}$ and the C/O ratio in C-rich AGB stars of $M_{\rm ini}$ = 2 and 3 M$_{\odot}$ with $Z_{\rm ini} \leq 10^{-4}$ are much larger than the values considered in the dust-driven wind models for C-rich AGB stars with solar and subsolar metallicities (e.g. Winters et al. 2000; Wachter et al. 2002, 2008; Mattsson, Wahlin & Höfner 2010).

3.2 Effective temperature

Fig. 3 shows the time evolution of effective temperature for the same models as presented in Fig. 1; note that the huge spikes of effective temperature during the TPs in the CNO-enhanced models with smaller current stellar mass are artificial, being associated with convergence problems. Owing to the very short duration of TPs, in which the effective temperature changes quickly, we will focus on the behaviour of effective temperature in the interpulse phases in what follows.

The effective temperature does not decrease below 3900 K in the scaled-solar models, regardless of the initial mass and metallicity (see Table 1); conversely, in the CO-enhanced and CNO-enhanced models, the time evolution of the effective temperature depends strongly on the initial mass, which determines the change in elemental composition in the surface regions during the TP-AGB phase. The effective temperature of the $M_{\rm ini} = 2$ M$_{\odot}$ star decreases with time more rapidly in the CNO-enhanced model than in the CO-enhanced model; the minimum values reached are $T_{\rm eff,min} = 3627$ and 3153 K in the CO-enhanced and CNO-enhanced models with $Z_{\rm ini} = 10^{-7}$, respectively. Generally speaking, the minimum effective temperature reached by a model of given mass is larger for smaller metallicity. The only exception to this trend is the $Z_{\rm ini} = 10^{-4}$ CNO-enhanced model. It should be remarked here that, even if the abundance of N in the surface layer is not enhanced without HBB, the CN molecule dominates the low-temperature opacity and decreases the effective temperature efficiently, since the first TDU and carbon ingestion (see Siess, Livio & Lattanzio 2002; Lau, Stancliffe & Tout 2009) increase the surface abundance of N in the AGB stars evolved from extremely metal-poor stars considered in this article. We note that the higher $T_{\rm eff,min}$ of the $Z_{\rm ini} = 10^{-4}$ model comes from the fact that the model does not experience carbon ingestion.

In the CO-enhanced models with $M_{\rm ini} = 3$ M$_{\odot}$, we can see from Fig. 3 that the effective temperature decreases with time in the initial C-rich phase, but increases after the onset of HBB. In the O-rich phase, when stronger HBB operates together with TDU, the effective temperature in the CO-enhanced models with $M_{\rm ini} = 3$ and 4 M$_{\odot}$ is almost the same as that in the scaled-solar models at the same current stellar mass. After HBB ceases, the effective temperature decreases with time in the C-rich phase, until the minimum value is reached. On the other hand, in the CNO-enhanced model, the effective temperature decreases with time efficiently even if HBB makes the surface layer O-rich, as can be seen from the time evolution of effective temperature for $M_{\rm ini}$ = 4 M$_{\odot}$ with CNO-enhanced opacity. This is because, even in O-rich environments, the enhancement of N increases the opacity through the CN molecule as demonstrated by Lederer & Aringer (2009) and thus the stellar radius.

Thus, even in the extremely metal-poor stars considered in this article, the employment of the low-temperature opacity, appropriately taking into account the change of elemental composition, such as the CNO-enhanced opacity, is inevitable to investigate the evolution of a star during the TP-AGB phase. Furthermore, as demonstrated in the next section, the treatment of the low-temperature opacity definitely influences the formation of carbon dust and the resulting gas outflow around AGB stars with $Z_{\rm ini} \leq 10^{-4}$.

4 FORMATION OF CARBON DUST AND RESULTING MASS LOSS

As presented in the previous section, all the models other than $M_{\rm ini} = 5$ M$_{\odot}$ with $Z_{\rm ini} = 0$ and 10^{-7} satisfy the minimum requirement for formation of carbon dust on the AGB after the stellar mass decreases below $M_{\rm C/O>1}$. However, not only $\delta_{\rm C}$ but also the effective temperature during the TP-AGB phase strongly influences the formation of carbon dust and the consequent DDW (see Gail & Sedlmayr 2013). In addition, Winters et al. (2000), based on hydrodynamical calculations of the DDW, showed that C-rich stars with stable gas outflows dominated by the effects of radiation pressure on dust with time-averaged radiative acceleration $\langle\alpha\rangle > 1$ experience mass-loss rates $\dot{M} \gtrsim 3 \times 10^{-7}$ M$_{\odot}$ yr^{-1}.

The present results, based on hydrodynamical calculations, show that CO-enhanced and CNO-enhanced models with $T_{\rm eff} \lesssim 4000$ K

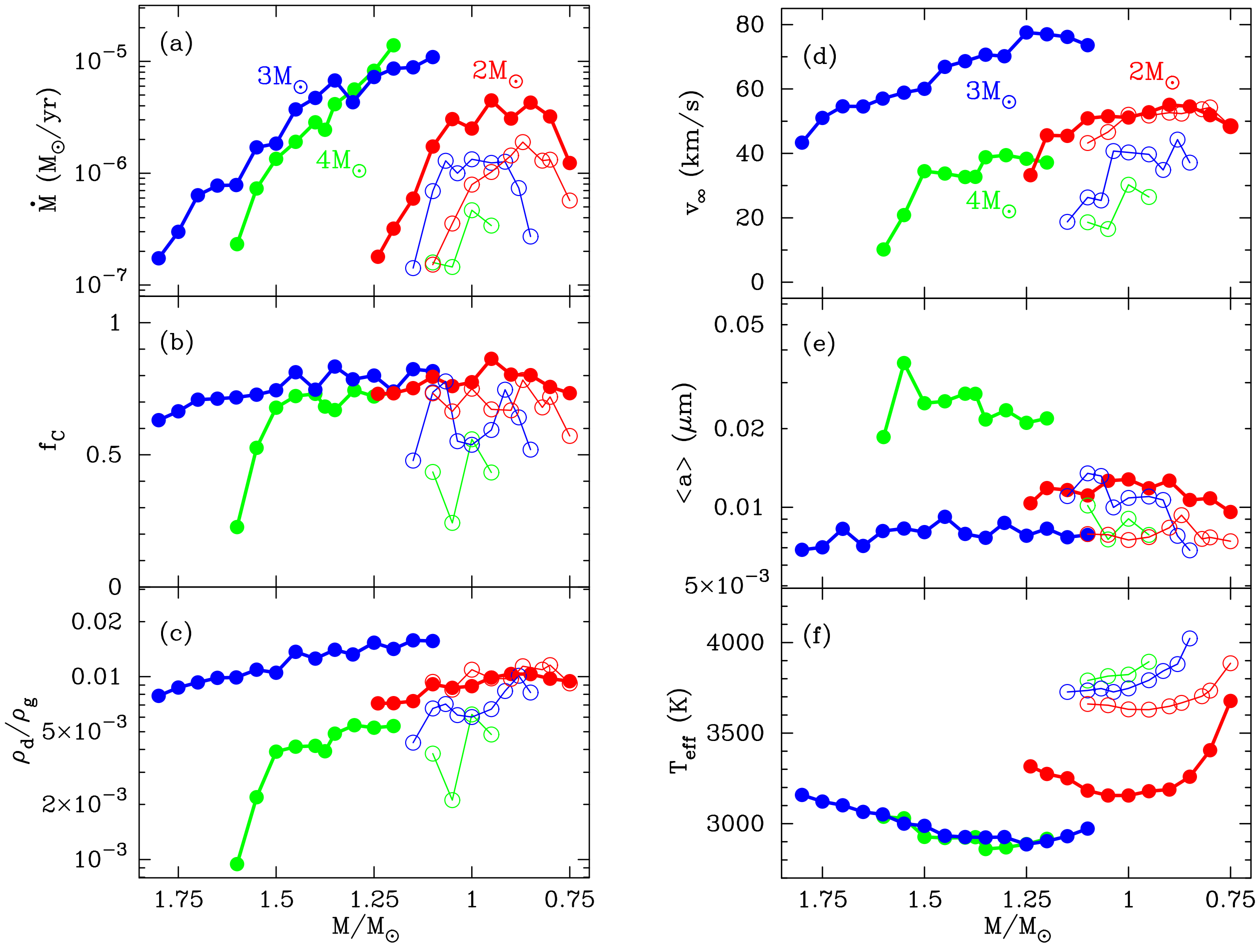

Figure 4. The effect of low-temperature opacity on dust formation and dust-driven wind and its dependence on the initial mass as a function of current stellar mass: from top to bottom, (a) mass-loss rate $\dot{M}$, (b) condensation efficiency of carbon $f_{\rm c}$, (c) dust-to-gas mass ratio $\rho_{\rm d}/\rho_{\rm g}$, (d) terminal wind velocity v_∞, (e) mass-averaged radius of dust $\langle a\rangle$ during the C-rich TP-AGB phase calculated by the hydrodynamical model of DDW and (f) effective temperature $T_{\rm eff}$ for the CO-enhanced (open circle – thin solid line) and CNO-enhanced (filled circle – thick solid line) models of $M_{\rm ini}$ = 2 (red), 3 (blue) and 4 M$_\odot$ (green) with $Z_{\rm ini} = 10^{-7}$.

develop a DDW with $\dot{M} > 10^{-7}$ M$_\odot$ yr^{-1} and $\langle\alpha\rangle > 1$ (hereinafter the stable DDW), except for the CO-enhanced models of $M_{\rm ini}$ = 4 M$_\odot$ with $Z_{\rm ini}$ = 0 and 5 M$_\odot$ with $Z_{\rm ini} = 10^{-5}$. On the other hand, the mass-loss rate of almost all scaled-solar models with $T_{\rm eff} > 4000$ K, excluding a few model stars, is limited to less than 10^{-7} M$_\odot$ yr^{-1} though $\langle\alpha\rangle > 1$. The scaled-solar opacity, not reflecting the change of elemental composition in the surface regions during the TP-AGB phase, could be inadequate in the low-temperature regime. Thus, in this section, focusing on the CO-enhanced and CNO-enhanced models with $\dot{M} \geq 10^{-7}$ M$_\odot$ yr^{-1} (stable DDW), we shall show the dependence of the formation of carbon dust and the consequent DDW around AGB stars on the treatment of low-temperature opacity as well as on the initial mass and metallicity. The input parameters used in the hydrodynamical calculations and the derived properties of DDW for the CO-enhanced and CNO-enhanced models are summarized in Appendix A: Table A1 for $Z_{\rm ini} = 10^{-7}$ and Table A2 for the other initial metallicities.

4.1 Effect of the low-temperature opacity and its dependence on the initial mass

Fig. 4 displays the time-averaged physical quantities characterizing dust formation and the consequent DDW, together with the effective temperature as a function of the current stellar mass for CO-enhanced and CNO-enhanced models of $M_{\rm ini}$ = 2, 3 and 4 M$_\odot$ with $Z_{\rm ini} = 10^{-7}$.

First, it should be pointed out that the formation of carbon dust and the resulting mass outflow do not operate in the C-rich phases alternating with O-rich phases associated with HBB, since the carbon excess $\delta_{\rm C} < 10^{-4}$ is insufficient and the effective temperature is too high to form carbon dust in a dense gas region close to the photosphere; formation of carbon dust occurs in regions where the temperature is below ∼1500 K (e.g. Yasuda & Kozasa 2012). Also, in the case of $M \gtrsim 2$ M$_\odot$, the larger gravitational force could prevent the star from driving gas outflow stably through the radiation pressure force acting on dust. Thus, the effective formation of carbon dust to drive the mass loss is activated only after the stellar mass is significantly reduced from the threshold stellar mass $M_{\rm C/O>1}$, as described below.

The general trend shown in Fig. 4 is that as the mass of the star decreases the mass-loss rate becomes larger, while the effective temperature decreases. This behaviour continues for a while even after the minimum effective temperature is reached. During the very final evolutionary phases, when the effective temperature increases rapidly, owing to peeling of the external layers, the mass-loss rate and dust condensation efficiency decline.

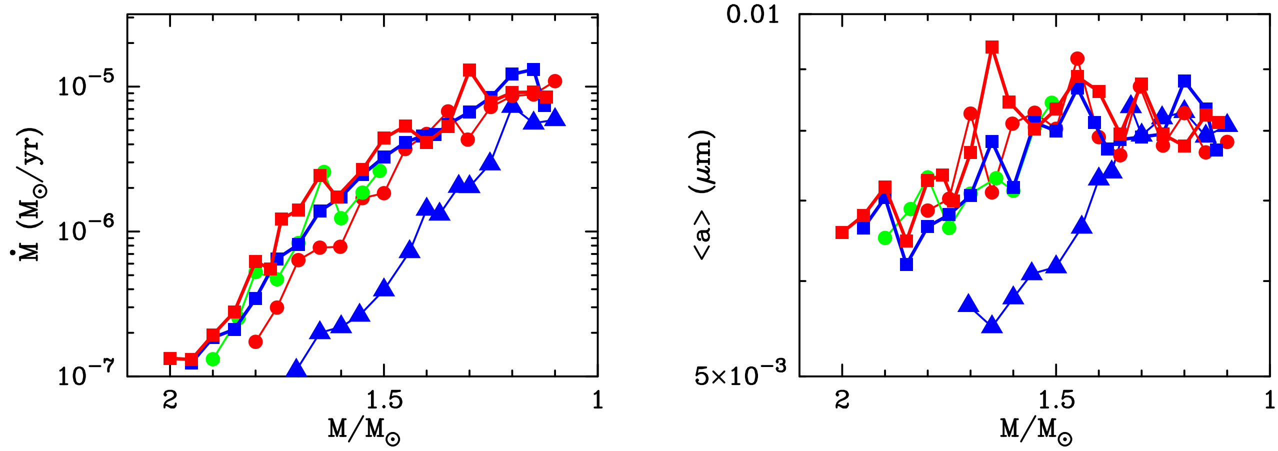

Figure 5. The dependence of the mass-loss rate (left panel) and the time-averaged mass-weighted radius of carbon dust (right) on the initial metallicity for the CNO-enhanced model with $M_{\rm ini} = 3\,{\rm M}_\odot$. The symbol and colour denote the metallicity: filled red square, blue square, green circle, red circle and blue triangle for $Z_{\rm ini} = 10^{-4}$, 10^{-5}, 10^{-6}, 10^{-7} and 0, respectively.

This trend of mass-loss rate holds irrespective of the treatment of low-temperature opacity. However, the value of the mass-loss rate, as well as the current stellar mass at which the stable DDW onsets, is heavily influenced by the treatment of low-temperature opacity, depending on the initial mass.

In the case of $M_{\rm ini} = 3\ {\rm M}_\odot$, the current stellar mass at the onset of a stable DDW and the maximum value of mass-loss rate are remarkably different between the CNO-enhanced and CO-enhanced models (see Fig. 4a); as shown in Section 3.2, the large value of surface opacity causes the photosphere to expand and suppresses the increase in temperature in the innermost layers of the convective envelope. Although HBB occurs in both models, the CNO-enhanced model undergoes much weaker HBB than the CO-enhanced model and HBB ceases at $\sim$2.0 ${\rm M}_\odot$ in the CNO-enhanced model and at $\sim$ 1.4 ${\rm M}_\odot$ in the CO-enhanced model. Then, the CNO-enhanced model evolving at smaller effective temperatures and reaching higher values of $\delta_{\rm C}$ activates the formation of carbon dust in denser regions, to drive the stable gas outflow at $M = 1.8\ {\rm M}_\odot$; in the CO-enhanced model, dust formation begins only after the mass of the stars decreases to $M \sim 1.2\ {\rm M}_\odot$. The mass-loss rate at the maximum is almost one order of magnitude smaller in the CO-enhanced model than in the CNO-enhanced model. On the other hand, the average radius of carbon dust is slightly smaller for the CNO-enhanced model, since more seed nuclei are produced in the outflowing gas, which accelerated efficiently owing to larger values of $\rho_{\rm d}/\rho_{\rm g}$.

The behaviour of the 4-${\rm M}_\odot$ models is different in comparison with their 3-${\rm M}_\odot$ counterparts: both models experience active HBB, since the core grows massive ($\sim$0.85 ${\rm M}_\odot$), and HBB ceases at $\sim$1.8 (1.4) ${\rm M}_\odot$ for the CNO (CO)-enhanced model. In the following phases in the CNO-enhanced model, the decrease in effective temperature leads to the onset of stable DDW when the mass is $\sim$1.6 ${\rm M}_\odot$ and the mass-loss rate increases sharply above $10^{-5}\ {\rm M}_\odot\ {\rm yr}^{-1}$. On the other hand, in the CO-enhanced model evolving at higher effective temperatures, the onset of a stable DDW is delayed to $M \sim 1.1\ {\rm M}_\odot$ and the largest mass-loss rate experienced is $\sim$5 $\times$ 10^{-7} ${\rm M}_\odot$ ${\rm yr}^{-1}$. It should be noted that the terminal gas velocity and dust-to-gas mass ratio in the CNO-enhanced model are considerably smaller in comparison with the CNO-enhanced model of $M_{\rm ini} = 3\ {\rm M}_\odot$, despite the fact that the mass-loss rate is comparable in both models for $M \lesssim 1.5\ {\rm M}_\odot$. This arises from the smaller value of $\delta_{\rm C}$, due to the delayed onset of effective dredge-up of carbon starting at $M \sim 1.8\ {\rm M}_\odot$. Thus, the slower gas outflow velocity allows dust grains to grow larger and results in a mass-weighted average radius more than a factor of 2 larger than that in the other models.

In the $M_{\rm ini} = 2\ {\rm M}_\odot$ models evolving without suffering HBB, the carbon excess $\delta_{\rm C}$ increases monotonically and gets larger in the CO-enhanced model than in the CNO-enhanced model as the stellar mass decreases (see Fig. 1). On the other hand, the effective temperature at the same current stellar mass is significantly lower in the CNO-enhanced model and the difference increases during the evolution. Thus, the gas density in the region of carbon dust formation as well as gas acceleration is higher in the CNO-enhanced model than in the CO-enhanced model. Although the condensation efficiency is a little smaller in the CO-enhanced model, the larger value of $\delta_{\rm C}$ makes the dust-to-gas mass ratio almost comparable in both models, as well as the gas terminal velocity being roughly proportional to $\rho_{\rm d}/\rho_{\rm g}$. The higher gas density of the dust-formation region results in a larger mass-loss rate in the CNO-enhanced model than in the CO-enhanced model (see Fig. 4a). However, being different from the cases of $M_{\rm ini} = 3$ and 4 ${\rm M}_\odot$, the difference in mass-loss rate between the CO-enhanced and CNO-enhanced models remains less than a factor of 3 at $M \lesssim 1\ {\rm M}_\odot$.

4.2 Dependence on the initial metallicity

The properties of the DDW, as well as the newly-formed carbon dust around AGB stars with $Z_{\rm ini} \leq 10^{-4}$, are expected not to depend directly on the initial metallicity, since the dredge-up carbon is of secondary origin and thus independent of $Z_{\rm ini}$. Fig. 5 displays the dependence of the mass-loss rate (left panel) and mass-weighted average radius of dust (right panel) on the initial metallicity for CNO-enhanced models of $M_{\rm ini} = 3\,{\rm M}_\odot$ with $Z_{\rm ini} = 10^{-4}$ (red square), 10^{-5} (blue square), 10^{-6} (green circle), 10^{-7} (red circle) and 0 (blue triangle).

We can see from Fig. 5 that, except for $Z_{\rm ini} = 0$, the mass-loss rates are almost the same at a given current stellar mass and any clear dependence on the initial metallicity is not recognized, apart from some fluctuations. This is also true for the mass-weighted radius of carbon dust; regardless of the initial metallicity, the radii, with a few exceptions, have almost the same value at a given current stellar mass and tend to increase slightly with decreasing current stellar mass. On the other hand, in the $Z_{\rm ini} = 0$ case, the mass-loss rate at

$M \gtrsim 1.2\,\mathrm{M}_\odot$ as well as the radius at $M \gtrsim 1.4\,\mathrm{M}_\odot$ is significantly smaller in comparison with the values for $10^{-7} \le Z_{\rm ini} \le 10^{-4}$. This difference reflects the fact that the higher effective temperature of a $Z_{\rm ini} = 0$ star without enrichment of N due to HBB (see Tables A1, A2, Section 3.2.2 and Fig. 2) during the AGB phase prevents carbon dust from forming in a dense region close to the photosphere. Thus, although the initial metallicity may subtly influence the properties of DDW and newly-formed carbon dust through its effects on stellar evolution, the present results demonstrate that carbon dust formation and the DDW do not show any significant dependence on the initial metallicity, as long as $10^{-7} \le Z_{\rm ini} \le 10^{-4}$.

In summary, the treatment of low-temperature opacity strongly affects dust formation and the consequent DDW on TP-AGB through its effect on the surface elemental composition and effective temperature, depending on the initial stellar mass. The current stellar mass at the onset of a stable DDW is considerably smaller ($\sim$1 $\mathrm{M}_\odot$) in the CO-enhanced model in comparison with that in the CNO-enhanced model. The largest mass-loss rate in the CO-enhanced model is at least one order of magnitude smaller than in the CNO-enhanced model, except for the case of $M_{\rm ini} = 2\,\mathrm{M}_\odot$, which does not experience HBB. Thus, the adoption of a low-temperature opacity varying with the change of elemental composition at the surface during the TP-AGB phase is inevitable to investigate dust formation and mass loss around AGB stars with extremely low initial metallicity, as considered in this article.

The mass-weighted radius of carbon dust formed in the outflowing gas is of the order of 0.01 μm, regardless of the treatment of low-temperature opacity as well as the initial mass and metallicity, except for the models of $M_{\rm ini} = 4$ and $5\,\mathrm{M}_\odot$ with the CNO-enhanced opacity developing slow and denser winds ($\langle a \rangle \sim 0.03$ μm). The derived radius of carbon dust is significantly smaller than the typical radius of carbon dust necessary for reproducing the colours of obscured C-rich AGB stars observed in the Magellanic Clouds; based on the stellar evolution calculations and the dust formation calculations employing the scheme developed by Ferrarotti & Gail (2006), typical radii of carbon dust are 0.06–0.2 μm in the Magellanic Clouds, assuming the number ratio of seed particles to hydrogen nuclei $n_{\rm s}/n_{\rm H} = 10^{-13}$ (Dell'Agli et al. 2015a, b), and 0.035–0.06 μm in the Small Magellanic Cloud (SMC), by varying $n_{\rm s}/n_{\rm H}$ up to 10^{-11} (Nanni et al. 2016). The assumed/considered values of $n_{\rm s}/n_{\rm H}$ in their models are considerably smaller than the values calculated in the present DDW models ($7 \times 10^{-12} \le n_{\rm s}/n_{\rm H} \le 10^{-8}$, depending on the initial mass as well as the input stellar parameters). Accordingly, the derived size of carbon dust is smaller, being roughly proportional to $(n_{\rm H}/n_{\rm s})^{1/3}$. Since the aim of this article is not to construct a self-consistent model with stellar evolution, comparison with observations is beyond the scope of this article.

5 DISCUSSION

The hydrodynamical calculations of the DDW in the previous section clearly demonstrate that the treatment of low-temperature opacity strongly affects dust formation and the resulting mass loss. Although the CNO-enhanced opacity is the most appropriate one among the three types of opacity considered, it should be remarked that the hydrodynamical model of the DDW employed in this article derives the properties of the DDW once a set of stellar parameters is given, as mentioned in Section 2.2 and presented in Section 3. Thus, irrespective of the mass-loss rate and the low-temperature opacity assumed in the stellar evolution calculations, the results of hydrodynamical calculation of the DDW along the evolutionary track on the AGB enable us to investigate the dependence of the properties of the DDW on the input stellar parameters; the ranges covered by the CNO-enhanced and CO-enhanced models with $\dot{M} \ge 10^{-7}\,\mathrm{M}_\odot\,\mathrm{yr}^{-1}$ are 2693 $< T_{\rm eff}/\mathrm{K} < 4037$, $1.23 < L/10^4\,\mathrm{L}_\odot < 3.23$, $0.7 \le M/\mathrm{M}_\odot \le 2.04$, $3.28 < \delta_{\rm C} \times 10^4 < 27.0$ and $1.50 < \kappa_{\rm R}/\mathrm{cm^2\,g^{-1}} \times 10^4 < 90.0$.

In this section, based on the results of DDW calculation presented in the previous section, we shall derive and discuss a condition necessary for an efficient DDW with $\dot{M} \ge 10^{-6}\mathrm{M}_\odot\,\mathrm{yr}^{-1}$ and the analytic formulae for gas and dust mass-loss rates in terms of the input stellar parameters. Furthermore, the implication for the evolution of intermediate-mass stars with $Z_{\rm ini} \le 10^{-4}$ in the early Universe is discussed in connection with dust formation and mass loss.

5.1 A necessary condition for an efficient dust-driven wind

The thresholds of the stellar parameters for the stable DDW around C-rich AGB stars with solar metallicity have been investigated by means of hydrodynamical calculations. Based on the range of stellar parameters inferred from observations of galactic carbon stars, Winters et al. (2000) found critical values of the various parameters for producing a stable DDW, depending on a combination of all the other parameters used in the hydrodynamical model. However, no attempt has been made to express the dependence explicitly in terms of the other parameters. Also, the hydrodynamical calculations by Winter et al. (2000) are confined to a narrower range of stellar parameters, especially for $T_{\rm eff}$ and $\delta_{\rm C}$, compared with the range covered by the present calculations. Thus, it is instructive to attempt at constraining of the conditions necessary for driving the DDW as a combination of stellar parameters, based on the present results.

First, it should be noted that the assumption of position coupling (drift velocity of dust is set to be 0) and the setting of velocity amplitude $\Delta u_{\rm P} = 2\,\mathrm{km\,s^{-1}}$ in the hydrodynamical model may influence the calculated mass-loss rates. Although Winters et al. (2000) have shown that the dependence of $\Delta u_{\rm P}$ on the mass-loss rate is weak as long as $\dot{M} \gtrsim 3 \times 10^{-6}\,\mathrm{M}_\odot\,\mathrm{yr}^{-1}$, at the present time little is known about the value of $\Delta u_{\rm P}$ allowed for C-rich AGB stars (Gail & Sedlmayr 2013). As for the assumption of position coupling, the recent two-fluid hydrodynamic model of the DDW considering dust formation as well as the interaction between gas and dust has demonstrated that the properties of the DDW are well reproduced by assuming position coupling for $\dot{M} \gtrsim 10^{-6}\,\mathrm{M}_\odot\,\mathrm{yr}^{-1}$ (Yasuda et al., in preparation). Thus, the calculated properties of a DDW with $\dot{M} \gtrsim 10^{-6}\,\mathrm{M}_\odot\,\mathrm{yr}^{-1}$ would not suffer significantly from the uncertainties arising from the assumption of position coupling underlying the hydrodynamical model used in the present article. Here, referring to the DDW with $\dot{M} \ge 10^{-6}\,\mathrm{M}_\odot\,\mathrm{yr}^{-1}$ as the efficient DDW in the following, we shall constrain the condition for producing the efficient DDW.

Among the stellar parameters used in the hydrodynamical model, the effective temperature is the most relevant parameter for the DDW, as discussed in previous studies (e.g. Winters et al. 2000, Wachter et al. 2002). The efficiency of gas acceleration due to radiation pressure on dust grains is roughly proportional to $\delta_{\rm C} L/M$. Also, the Rosseland mean opacity $\kappa_{\rm R}$ at the photosphere, which controls the density structure of the surface regions, is considered to have a significant effect on the DDW, in connection with the density of gas levitated by the pulsation shock.

Fig. 6 shows $\Lambda = \delta_{\rm C} L/\kappa_{\rm R} M$ versus $T_{\rm eff}$ for the CNO-enhanced and CO-enhanced models tabulated in Appendix A. The dotted lines indicate the boundaries on the $\log T_{\rm eff}$–$\log \Lambda$ plane for the

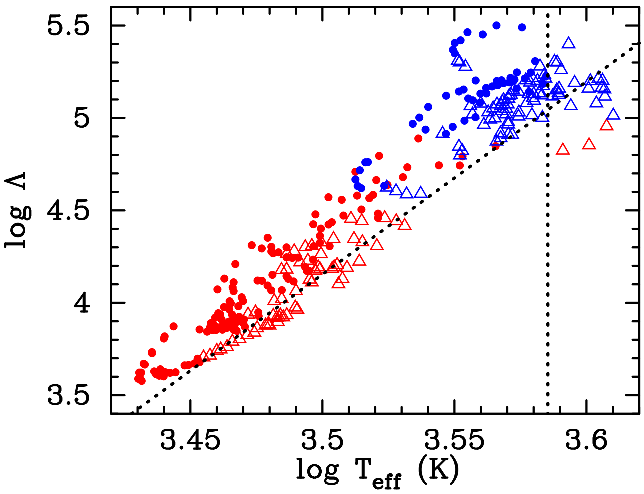

Figure 6. The plot of $\Lambda = \delta_{\rm C} L/\kappa_{\rm R} M$ versus $T_{\rm eff}$, with M and L in solar units and $\kappa_{\rm R}$ in units of cm^2 g^{-1}; the red (blue) filled circle is for the CNO (CO)-enhanced model with $\dot{M} \geq 10^{-6}$ M$_\odot$ yr^{-1} and the red (blue) open triangle for the CNO (CO)-enhanced model with $\dot{M} < 10^{-6}$ M$_\odot$ yr^{-1}. The dotted lines represent the boundaries for the possible formation of a DDW with $\dot{M} \geq 10^{-6}$ M$_\odot$ yr^{-1}.

possible formation of an efficient DDW. From this plot, we can see that efficient DDW is possible only if $T_{\rm eff} \lesssim 3850$ K and $\log \Lambda \gtrsim 10.34 \log T_{\rm eff} - 32.33$, though the boundary seems to reflect the TP-AGB tracks of the models somewhat. Although the derived constraint condition is only a necessary condition, the condition could be useful for judging when the efficient DDW resulting from the formation of carbon dust onsets in the course of evolution of C-rich AGB stars, by referring to the stellar parameters along the evolutionary track derived by the stellar evolution calculation.

5.2 Analytic formulae for gas and dust mass-loss rates

The amount of gas and dust that C-rich AGB stars supply to interstellar space is crucial not only to reveal the origin of dust but also to investigate the formation and evolution of stars in galaxies through chemical evolution models in the early Universe (e.g. Grieco et al. 2014). Formulae for the mass-loss rate for C-rich AGB stars with solar and subsolar metallicities have been proposed, based on hydrodynamical calculations of the DDW (Arndt, Fleischer & Sedlmayr 1997; Wachter et al. 2002, 2008). Although Weiss & Ferguson (2009) applied the formula by Wachter et al. (2002) to investigate the evolution of stars with $Z_{\rm ini} = 5 \times 10^{-4}$–0.04, it is questionable whether the same formula can be applied to C-rich AGB stars of metallicity $Z_{\rm ini} \leq 10^{-4}$. Here, we shall derive the analytic formulae for gas and dust mass-loss rates in terms of the input stellar parameters employed in the hydrodynamical calculations for CNO-enhanced and CO-enhanced models with the efficient DDW.

For simplicity, we derive the formulae under the assumption that the mass-loss rate is simply approximated by a linear function of the logarithms of the input parameters (M, L, $T_{\rm eff}$, $\kappa_{\rm R}$, $\delta_{\rm C}$ and P). Also, we shall consider the initial metallicity as a parameter, since the mass-loss rates of the $Z_{\rm ini} = 0$ models deviate from the others (see the left panel of Fig. 5), though the mass-loss rates of stars with $10^{-7} \leq Z_{\rm ini} \leq 10^{-4}$ do not show a clear dependence on the initial metallicity. Applying the least-squares method to the mass-loss rates and the dust-to-gas mass ratios tabulated in Appendix A, the fitting formula is expressed as

$$\log \dot{M}_{\rm fit} = a + b \log\left(\frac{T_{\rm eff}}{3000\,{\rm K}}\right) + c \log\left(\frac{L}{10^4\,{\rm L}_\odot}\right) + d \log\left(\frac{M}{{\rm M}_\odot}\right) + e \log\left(\frac{\delta_{\rm C}}{10^{-4}}\right) + f \log\left(\frac{\kappa_{\rm R}}{10^{-4}{\rm cm}^2\,{\rm g}^{-1}}\right) + g \log\left(\frac{P}{650\,{\rm d}}\right) + h \log Z_{\rm ini}. \quad (3)$$

Note that we adopt $Z_{\rm ini} = 10^{-12}$ as representative of $Z_{\rm ini} = 0$ when fitting. The numerical coefficients from a to h for the formulae for gas (dust) mass-loss rate $\dot{M}^{\rm g}_{\rm fit}$ ($\dot{M}^{\rm d}_{\rm fit}$) with and without including the initial metallicity are provided in Table 2, with correlation coefficient R and maximum deviation D from the calculated values. The formula for the gas (dust) mass-loss rate not including metallicity fits the values calculated by the DDW model with correlation coefficient 0.87 (0.92) and maximum deviation 38 (50) per cent. The fittings are only slightly improved by including the metallicity, reflecting the fact that the mass-loss rate does not depend sensitively on the initial metallicity, with coefficient $h \sim 0.02$–0.03.

The power of the effective temperature in the gas mass-loss formula is huge (e.g. $b = -19.13$ for the case without $Z_{\rm ini}$) in comparison with that in the formulae by Wachter et al. (2008, hereafter W08). The huge power arises from the inclusion of $\delta_{\rm C}$ and $\kappa_{\rm R}$ in the fitting formula. In fact, the gas mass-loss rate being fitted by using M, L and $T_{\rm eff}$ in the same manner as W08, the formula is given by $\dot{M}^{\rm g}_{\rm fit} = 7.62 \times 10^{-6} (M/{\rm M}_\odot)^{-4.28} (T_{\rm eff}/2600\,{\rm K})^{-7.64} (L/10^4\,{\rm L}_\odot)^{1.66}$ with correlation coefficient 0.80 and maximum deviation 42 per cent. Thus, the power of the effective temperature is reduced to -7.64, comparable with the value in the formula by W08. Here it should be noted that the inclusion of $\delta_{\rm C}$ and $\kappa_{\rm R}$ is inevitable in the fitting formula, since $\delta_{\rm C}$ and $\kappa_{\rm R}$ control the amount of carbon available for dust formation and the density of gas levitated by the pulsation shock, respectively.

Fig. 7 shows the evolution of the gas mass-loss rate of the CNO-enhanced models with $Z_{\rm ini} = 10^{-7}$; $M_{\rm ini} = 2$ M$_\odot$ (left) and 3 M$_\odot$ (right). The mass-loss rates calculated by the DDW model and the fitting formula without including metallicity are denoted by the filled circles and the solid line, respectively, with dotted and dashed lines indicating the results obtained by assuming, respectively, the mass-loss formulae by W08 for the SMC models and SC05. We can see that the fitting formula equation (3) reproduces the mass-loss rates derived from the DDW model reasonably, as long as $\dot{M} \gtrsim 10^{-6}$ M$_\odot$ yr^{-1} in both models.

As shown in Fig. 7, the mass-loss rate assuming the formula for the SMC models by W08 is more than one order of magnitude larger than the rate calculated for C-rich AGB stars with $Z_{\rm ini} = 10^{-7}$. Although the difference in the stellar parameters used in the calculations makes it difficult to compare the results directly, the gap in the calculated mass-loss rate is caused by differences in the Rosseland mean opacity $\kappa_{\rm R}$ at the surface and the amplitude of pulsation $\Delta u_{\rm P}$: $\kappa_{\rm R} = 5 \times 10^{-5}$ cm^2 g^{-1} and $\Delta u_{\rm P} = 5$ km s^{-1} for the SMC models in W08; $\kappa_{\rm R} = {\sim}10^{-3}$ cm^2 g^{-1} as a typical value (see Table A1) and $\Delta u_{\rm P} = 2$ km s^{-1} in the CNO-enhanced models with $Z_{\rm ini} = 10^{-7}$. The difference in the value of $\kappa_{\rm R}$ implies that the gas density in the surface region, being roughly proportional to $\kappa_{\rm R}$, is a factor of 20 larger in the SMC models than in the CNO-enhanced models. Also, the carbon excess $\delta_{\rm C} = 8.57 \times 10^{-5}$ in the SMC models, assuming C/O=1.8 and taking the oxygen abundance from Russell & Dopita (1992), while $\delta_{\rm C} \sim 10^{-3}$ as a typical value in the CNO-enhanced models investigated here. Although the amount of carbon in the surface layer is comparable, the higher gas density in

Table 2. The coefficients of the mass-loss formulae (equation 3) of gas ($\dot{M}^{\rm g}_{\rm fit}$) and dust ($\dot{M}^{\rm d}_{\rm fit}$) for cases with and without $Z_{\rm ini}$ and their correlation coefficient R and maximum deviation D in per cent from the values calculated by the hydrodynamical model.

	a	*b*	*c*	*d*	*e*	*f*	*g*	*h*	*R*	*D* (per cent)
$\dot{M}^{\rm g}_{\rm fit}$ without $Z_{\rm ini}$	−5.733	−19.13	3.164	−5.254	0.7768	−0.7089	−0.8955	0	0.88	39
$\dot{M}^{\rm g}_{\rm fit}$ with $Z_{\rm ini}$	−5.590	−20.07	3.221	−5.182	0.8836	−0.8476	−0.8138	0.02220	0.90	34
$\dot{M}^{\rm d}_{\rm fit}$ without $Z_{\rm ini}$	−8.991	−19.21	2.874	−5.361	1.843	−0.6417	−0.8834	0	0.92	51
$\dot{M}^{\rm d}_{\rm fit}$ with $Z_{\rm ini}$	−8.822	−19.41	2.696	−5.075	1.977	−0.8163	−0.5075	0.02774	0.94	46

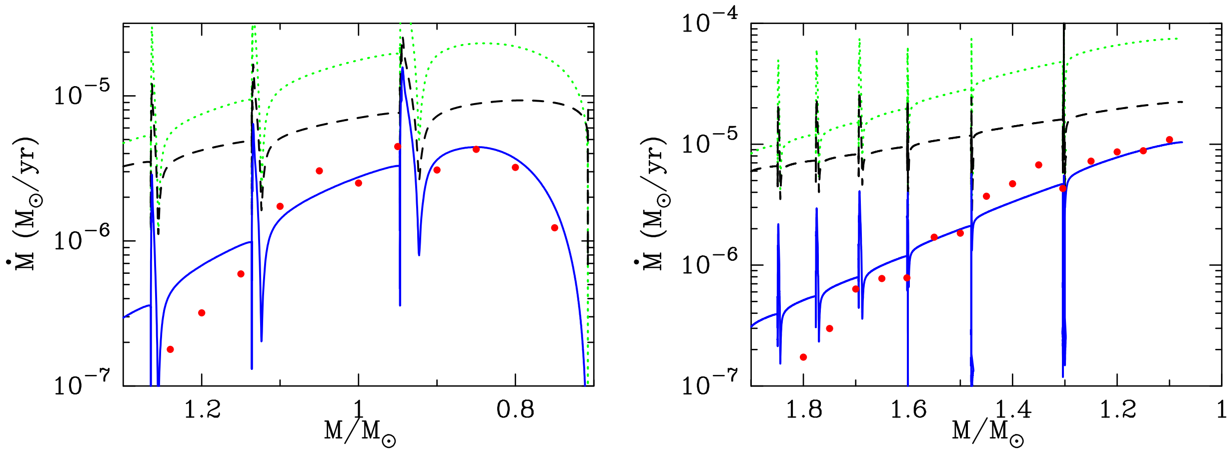

Figure 7. Time evolution of mass-loss rates for CNO-enhanced models with $M_{\rm ini} = 2$ (left panel) and 3 (right panel) $M_\odot$, with $Z_{\rm ini} = 10^{-7}$. The mass-loss rate calculated by the DDW model and the fitting formula (equation 3) are denoted by a red circle and solid line, respectively. The dotted (dashed) line shows the mass-loss rate calculated by the formula for the SMC models of W08 (SC05 assumed in the stellar evolution calculation) as a reference.

the surface region as well as the enhanced density of gas levitated by the pulsation shock with larger $\Delta u_{\rm P}$ leads to a larger mass-loss rate in the SMC models. Here, it should be addressed that the values of $\kappa_{\rm R}$ and $\delta_{\rm C}$ used in W08 seem to be unrealistic in comparison with the values derived from stellar evolution calculations and the applicability of their formula for C-rich AGB stars with $Z_{\rm ini} \le 10^{-4}$ should be checked by using the appropriate values. Also, the dependence of the mass-loss rate on the velocity amplitude of pulsation should be investigated, since the dependence is considered to be more sensitive for stars with larger $\delta_{\rm C}$ and $\kappa_{\rm R}$.

The mass-loss rate derived from the DDW model is significantly smaller than the mass-loss rate assumed in stellar evolution calculations. If we use the derived mass-loss formula after the necessary condition for the efficient DDW is satisfied on the TP-AGB, the dredged-up carbon accumulates in the surface regions; accordingly, the effective temperature decreases and the mass-loss rate could increase. Although in the present calculations the derived mass-loss rate is inconsistent with the assumed mass-loss rate, it should be recalled here again that the hydrodynamical model can derive the properties of the DDW by specifying a set of input parameters, being independent of the stellar evolution model. Thus, the derived formulae, together with a necessary condition for the efficient DDW presented in Section 5.1, could enable us to evaluate the mass-loss rate and dust yield during the C-rich AGB phase of stars with $Z_{\rm ini} \le 10^{-4}$ in a manner consistent with stellar evolution, including whether the efficient DDW can operate on the C-rich AGB.

5.3 Implication for evolution of C-rich AGB stars and the dust-driven wind in the early Universe

Investigations on the formation of stars in low-metallicity environments have revealed that the critical metallicity $Z_{\rm cri}$ for the transition from Population III to Population II stars is as low as $\sim 10^{-9}$–$10^{-7.5}$, depending on the depletion factor of metal into dust (e.g. Omukai et al. 2005, Schneider et al. 2006, Chiaki et al. 2015). Although there is no information available for the initial mass function at the present time, intermediate-mass AGB stars with $Z_{\rm ini} \le 10^{-4}$ can contribute to the enrichment of dust in the early Universe if the condition for the efficient DDW derived in the previous subsection is satisfied during the TP-AGB phase. However, the possibility of developing dust formation and a resulting DDW on the AGB is strongly influenced by the mass-loss history during the evolution, on which the time evolution of effective temperature as well as the elemental composition and opacity in the surface layer depend strongly through the number of TDU episodes and/or the occurrence of HBB. At present, we have no knowledge of the mass-loss mechanism and mass-loss rate before the onset of the DDW for the extremely low-metallicity stars considered in this article.

In recent investigations focused on low-metallicity ($-1.6 < $ [Fe/H] < -0.5) AGB stars observed in distant galaxies, Rosenfield et al. (2014, 2016) showed that a mass-loss rate higher than SC05 is required during the AGB phases previous to the onset of the DDW, to reproduce the observed TP-AGB luminosity function as well as the number ratio of TP-AGB to red giant stars. If this is true for the AGB phase of stars with $Z_{\rm ini} \le 10^{-4}$, the so-called pulsation enhanced DDW would not operate as the mass-loss mechanism; in stars losing mass efficiently on the AGB, the number of TDUs is reduced and the inefficient decrease of effective temperature as well as insufficient carbon excess ($\delta_{\rm C}$) prohibits the onset of dust formation and the efficient DDW. On the other hand, when the mass-loss rate in the pre-dust phase on the AGB is depressed, it is possible for the DDW to dominate the mass loss after the stellar mass is substantially reduced below $M_{\rm C/O>1}$, as demonstrated in Section 4. In cases such as $M_{ini} = 2\ M_\odot$ not experiencing any HBB, the increase in carbon excess and decrease in effective temperature could make the DDW more efficient. For stars of mass $M_{ini} \geq 3\ M_\odot$ that experience HBB, a smaller mass-loss rate on the AGB results in more active HBB that seems to decrease the threshold mass $M_{C/O>1}$ and the carbon excess in the C-rich phase. However, the enrichment of N in the surface layer associated with HBB can counteract HBB itself, since the enhanced surface opacity depresses the increase in gas temperature in the innermost layer of the convective envelope and makes HBB weaker. Thus, it can be expected that, even in massive stars experiencing HBB, mass loss by the DDW could operate, although the details depend on the initial mass and mass-loss rate in the pre-dust phase. Anyway, the present results of DDW calculations demonstrate that the formation of carbon dust and the resulting DDW is possible even in low-metallicity environments with $Z_{ini} \leq 10^{-4}$, as long as the mass-loss rate in the pre-dust phase on the AGB is reduced to some extent from the rate given by SC05.

Finally, it is useful to note the following in connection with the uncertainties inherent in the present DDW model. In section 4, the DDW with $\dot{M} \geq 10^{-7}\ M_\odot\ yr^{-1}$ is referred to as the stable DDW, according to Winters et al. (2000), since the time-averaged value $\langle\alpha\rangle \gtrsim 1$. However, in the present calculations, contrary to the results of Winters et al. (2000), we have not found any sustainable wind with $\langle\alpha\rangle < 1$, since the carbon excess δ_C of C-rich AGB stars with $Z_{ini} \leq 10^{-4}$ is significantly larger than the value inferred from observations of galactic C-rich AGB stars; $\delta_C \sim 6.76 \times 10^{-4}$, corresponding to C/O = 2.0 for solar metallicity. Also, recent investigation using the two-fluid hydrodynamic calculation for the DDW has shown that the assumption of position coupling will break down around $\dot{M} \sim$ several $\times\ 10^{-7}\ M_\odot\ yr^{-1}$ (Yasuda et al., in preparation). Thus, application of the two-fluid hydrodynamic model is inevitable to explore the constraint conditions for the onset of a stable DDW. In addition, although the velocity amplitude of pulsation Δu_p is set to be 2 km s^{-1}, the large δ_C and κ_R in the surface region may make the dependence of the value of Δu_p on the formation of carbon dust and the resulting DDW more sensitive than the case for Galactic C-rich stars; the increase of Δu_p up to 8 km s^{-1} (Winters et al. 2000) may enhance the mass-loss rate from the DDW substantially. These aspects should be investigated systematically in future works to explore the properties of the DDW and the nature of carbon dust formed around AGB stars in the early Universe, consistent with stellar evolution calculations.

6 SUMMARY

In order to explore dust formation and the resulting mass loss around intermediate-mass AGB stars with initial metallicity $Z_{ini} \leq 10^{-4}$ in the early Universe, hydrodynamical calculations of the dust-driven wind (DDW) are carried out for stars with initial mass in the range $2 \leq M_{ini}/M_\odot \leq 5$. The input stellar parameters necessary for the hydrodynamical calculation are calculated by the MESA code, assuming the mass-loss rate given by Schröder & Cuntz (2005) in the post-main-sequence phase as a first step for this study. In addition, three types of low-temperature opacity (scaled-solar, CO-enhanced and CNO-enhanced) are considered to elucidate the effect of the treatment of low-temperature opacity on the time evolution of stellar parameters related to the dust formation and consequent DDW.

We confirm that all model stars, except for $M_{ini} = 5\ M_\odot$ with $Z_{ini} = 0$ and 10^{-7}, finally turn out to be C-rich and satisfy the minimum condition for the formation of carbon dust, regardless of the treatment of low-temperature opacity. However, the effective temperature, the quantity most sensitive to the dust formation process, is strongly affected by the treatment of low-temperature opacity; the minimum effective temperature $T_{eff,min}$ in the interpulse phases does not decrease below 3900 K for stars with scaled-solar opacity, while $T_{eff,min}$ decreases below 3100 K for stars of $M_{ini} \geq 3 M_\odot$ with CNO-enhanced opacity.

Hydrodynamical calculations of the DDW along the evolutionary track of C-rich AGB stars simulated with CO-enhanced and CNO-enhanced opacities show the following. The stellar mass at which the stable DDW with $\dot{M} \geq 10^{-7}\ M_\odot\ yr^{-1}$ onsets is significantly smaller in the CO-enhanced model than in the CNO-enhanced models and the maximum mass-loss rate on C-rich AGB is more than one order of magnitude smaller in the CO-enhanced models than in the CNO-enhanced models for $M_{ini} \geq 3\ M_\odot$. Thus, the employment of composition-dependent low-temperature opacity, such as CNO-enhanced opacity, is inevitable to investigate the formation of dust and resulting mass loss in low-metallicity AGB stars. Also, we find that, given the initial mass, the time evolution of the mass-loss rate, as well as the time-averaged mass-weighted radius of carbon dust, is almost independent of the initial metallicity, as long as $10^{-7} \leq Z_{ini} \leq 10^{-4}$.

The results of the DDW calculation covering a wide range of stellar parameters, regardless of the treatment of low-temperature opacity and the mass-loss rate assumed in the stellar evolution calculations, enable us to derive a necessary condition for driving the efficient DDW with $\dot{M} \geq 10^{-6}\ M_\odot\ yr^{-1}$ as a combination of stellar parameters and the fitting formulae for gas and dust mass-loss rates in terms of input stellar parameters; the fitting formula for the gas mass-loss rate reproduces the mass-loss rate calculated by DDW model reasonably. The derived necessary condition and the fitting formulae would enable us to evaluate when the efficient DDW onsets and how much dust is produced in intermediate AGB stars with $Z_{ini} \leq 10^{-4}$, when coupled with the stellar evolution calculations.

The present results of calculations employing the mass-loss rate by SC05 in the post main-sequence phase suggest that the efficient DDW being consistent with the stellar evolution could be possible if the mass-loss rate during the evolution of a star were somewhat enhanced before entering into the AGB and depressed on the AGB before the onset of the DDW from the rate given by SC05. Also, it should be emphasized here that the assumption of position coupling is not valid for the case of a low mass-loss rate such as $\dot{M} \sim$ several $\times\ 10^{-7}\ M_\odot\ yr^{-1}$; the assumption of position coupling results in overestimation of the mass-loss rate of C-rich AGB stars with larger δ_C considered in this article, since $\dot{M} \propto \delta_C$. Thus, a two-fluid hydrodynamical model calculation of the DDW is necessary to clarify when and in what conditions the DDW actually onsets during the course of evolution of AGB stars. Also, large values of δ_C and κ_R may result in a sensitive dependence of mass-loss rate on the velocity amplitude of pulsation. These subjects are left for future investigations.

ACKNOWLEDGEMENTS

We thank the anonymous referee for detailed and thorough comments, which were very useful and helpful in improving the manuscript. This research has been partly supported by the Grant-in Aid for Scientific Research of the Japan Society for the Promotion of Science (23224004, 16H0218).

REFERENCES

Arndt T. U., Fleischer A. J., Sedlmayr E., 1997, A&A, 327, 614
Blöcker T., 1995, A&A, 297, 727
Campbell S. W., Lattanzio J. C., 2008, A&A, 490, 769
Canuto V. M. C., Mazzitelli I., 1991, ApJ, 370, 295
Chiaki G., Marrasi S., Nozawa T., Yoshida N., Schneider R., Omukai K., Limongi M., Chieffi A., 2015, MNRAS, 446, 2659
Constantino T., Campbell S., Gil-Pons P., Lattanzio J., 2014, ApJ, 784, 56
Cox J. P., Giuli R. T., 1968, Principles of Stellar Structure. Gordon and Breach, NY
Cristallo S., Straniero O., Lederer M. T., Aringer B., 2007, ApJ, 667, 489
Dell'Agli F., Ventura P., Schneider R., Di Criscienzo M., Garcia-Hernandez D. A., Rossi C., Brocato E., 2015a, MNRAS, 447, 2992
Dell'Agli F., Garcia-Hernandez D. A., Ventura P., Schneider R., Di Criscienzo M., Rossi C., 2015b, MNRAS, 454, 4235
Di Criscienzo M. et al., 2013, MNRAS, 433, 313
Draine B. T., 1985, ApJS, 57, 587
Dwek E., Galliano F., Jones A. P., 2007, ApJ, 662, 927
Ferrarotti A. S., Gail H.-P., 2006, A&A, 447, 553
Fishlock C. K., Karakas A. I., Stancliffe R. J., 2014, MNRAS, 438, 1741
Fleischer A. J., Gauger A., Sedlmayr E., 1992, A&A, 266, 321
Gail H.-P., Sedlmayr E., 2013, Physics and Chemistry of Circumstellar Dust Shells. Cambridge Univ. Press, Cambridge, UK
Gauger A., Gail H.-P., Sedlmayr E., 1990, A&A, 235, 345
Grevesse N., Noels A., 1993, Phys. Scr., T47, 133
Grieco V., Matteucci F., Calura F., Boissier S., Longo F., D'Elia V., 2014, MNRAS, 444, 1054
Herwig F., 2000, A&A, 360, 952
Herwig F., 2005, ARA&A, 43, 435
Iglesias C. A., Rogers F. J., 1993, ApJ, 412, 752
Iglesias C. A., Rogers F. J., 1996, ApJ, 464, 943
Karakas A., Lattanzio J. C., 2007, PASA, 24, 103
Lau H. H. B., Stancliffe R. J., Tout C. A., 2009, MNRAS, 396, 1046
Lederer M. T., Aringer B., 2009, A&A, 494, 403
Marigo P., 2002, A&A, 387, 507
Marigo P., Aringer B., 2009, A&A, 508, 1539
Mattsson L., Wahlin R., Höfner S., 2010, A&A, 509, A14
Nanni A., Bressan A., Marigo P., Girardi L., 2013, MNRAS, 434, 2390
Nanni A., Marigo P., Groenewegen M. A. T., Aringer B., Girardi L., Pastorelli G., Bressan A., Bladh S., 2016, MNRAS, 462, 1215
Nozawa T., Kozasa T., Umeda H., Maeda K., Nomoto K., 2003, ApJ, 598, 785
Omukai K., Tsuribe T., Schneider R., Ferrara A., 2005, ApJ, 626, 627
Ostlie D. A., Cox A. N., 1986, ApJ, 311, 864
Paxton B., Bildsten L., Dotter A., Herwig F., Lesaffre P., Timmes F., 2011, ApJS, 192, 3
Paxton B. et al., 2013, ApJS, 208, 4
Reimers D., 1975, Mem. Soc. R. Sci. Liege, 8, 369
Renzini A., Voli M., 1981, A&A, 94, 175
Rosenfield P. et al., 2014, ApJ, 790, 22
Rosenfield P., Marigo P., Girardi L., Dalcanton J. J., Bressan A., Williams B. F., Dolphin A., 2016, ApJ, 822, 73
Russell S., Dopita M. A., 1992, ApJ, 384, 508
Schneider R., Omukai K., Inoue A., Ferrara A., 2006, MNRAS, 369, 1437
Schröder K.-P., Cuntz M., 2005, ApJ, 630, L73
Schröder K.-P., Cuntz M., 2007, A&A, 465, 593
Siess L., Livio M., Lattanzio J., 2002, ApJ, 570, 329
Todini P., Ferrara A., 2001, MNRAS, 325, 736
Valiante R., Schneider R., Bianchi S., Andersen A. C., 2009, MNRAS, 397, 1661
Valiante R., Schneider R., Salvadori S., Bianchi S., 2011, MNRAS, 416, 1916
van Loon J. T., Cioni M.-R. L., Zijlstra A. A., Loup C., 2005, A&A, 438, 273
Vassiliadis E., Wood P. R., 1993, ApJ, 413, 641
Ventura P., D'Antona F., 2005, A&A, 431, 279
Ventura P., Marigo P., 2010, MNRAS, 408, 2476
Ventura P. et al., 2012a, MNRAS, 420, 1442
Ventura P. et al., 2012b, MNRAS, 424, 2345
Ventura P., Dell'Agli F., Schneider R., Di Criscienzo M., Rossi C., La Franca F., Gallerani S., Valiante R., 2014, MNRAS, 439, 977
Wachter A., Schröder K. -P., Winters J. M., Arndt. U., Sedlmayr E., 2002, A&A, 384, 452
Wachter A., Winters J. M., Schröder K. -P., Sedlmayr E., 2008, A&A, 486, 497 (W08)
Weiss A., Ferguson J. W., 2009, A&A, 508, 1343
Winters J. M., Le Bertre T., Jeong K. S., Helling Ch., Sedlmayr E., 2000, A&A, 361, 641
Wood P. R., 1986, in Cox A. N., Sparks W., Starrfield S., eds., Springer Lecture Notes in Physics No. 274, Stellar Pulsation. Springer-Verlag , Berlin, p. 250
Yasuda Y., Kozasa T., 2012, ApJ, 745, 159
Zhukovska S., Gail H.-P., Trieloff M., 2008, A&A, 479, 453

APPENDIX A: INPUT STELLAR PARAMETERS FOR HYDRODYNAMICAL CALCULATIONS AND THE DERIVED PROPERTIES OF DUST-DRIVEN WINDS

The input stellar parameters of hydrodynamical calculations and the derived properties of dust-driven winds are tabulated for CO-enhanced and CNO-enhanced models with mass-loss rate $\dot{M} \geq 10^{-7}$ $M_{\odot}$ yr^{-1}: Table A1 for $Z_{ini} = 10^{-7}$ and Table A2 for $Z_{ini} = 10^{-4}$, 10^{-5}, 10^{-6} and 0.

Table A1. Input parameters and derived properties of the dust-driven wind for $M_{ini} = 2$, 3 and 4 $M_\odot$ with $Z_{ini} = 10^{-7}$: current stellar mass M ($M_\odot$), effective temperature T_{eff} (K), luminosity L ($L_\odot$), pulsation period P (days), opacity (cm^2 g^{-1}), number ratio at the surface of He, C, O and N to H, current stellar mass M ($M_\odot$), time-averaged acceleration ratio $\langle\alpha\rangle$, mass-loss rate $\dot{M}$ ($M_\odot$ yr^{-1}), terminal velocity v_∞ (km s^{-1}), dust-to-gas mass ratio ρ_d/ρ_g, condensation efficiency f_C, mass-weighted average radius of dust $\langle a\rangle$ (μm).

M	T_{eff}	L	P	κ	He/H	C/H	O/H	N/H	δ_C	α	$\dot{M}$	v_∞	ρ_d/ρ_g	f_C	$\langle a\rangle$
$M_{ini} = 2\,M_\odot$, $Z_{ini} = 10^{-7}$				$\times 10^4$		$\times 10^3$	$\times 10^5$	$\times 10^5$	$\times 10^3$		$\times 10^7$		$\times 10^3$		$\times 10^3$
CNO-enhanced															
1.240	3316.05	12828.2	535.866	5.80808	0.107852	1.23789	9.74055	1.93039	1.14048	11.7731	1.78877	33.2258	7.14138	0.730532	10.353
1.200	3274.39	13458.4	602.060	6.00227	0.107852	1.23789	9.74055	1.93039	1.14048	16.0197	3.19385	45.6061	7.16348	0.732794	11.839
1.150	3250.59	13613.8	643.431	6.08223	0.107852	1.23789	9.74055	1.93039	1.14048	17.6043	5.92034	45.4434	7.35327	0.752208	11.637
1.100	3182.16	13187.4	700.316	7.89849	0.108914	1.44937	11.4939	1.97024	1.33443	20.9863	17.3274	50.8977	9.09215	0.794908	11.096
1.050	3155.38	13689.5	773.749	8.24118	0.108914	1.44937	11.4939	1.97024	1.33443	24.5245	30.4119	51.5424	8.69243	0.759962	12.622
1.000	3155.38	13832.9	807.880	8.01272	0.108914	1.44937	11.4939	1.97024	1.33443	26.8692	25.0564	51.1623	8.86184	0.774773	12.781
0.950	3179.18	13817.0	815.120	7.31592	0.108914	1.44937	11.4939	1.97024	1.33443	28.6445	44.7127	52.7775	9.87456	0.863313	11.826
0.900	3188.11	12988.2	792.366	7.94418	0.109937	1.63186	12.9682	2.04994	1.50218	32.6010	30.8123	55.1010	10.3428	0.803272	12.642
0.850	3259.52	13717.4	800.640	6.37923	0.109937	1.63186	12.9682	2.04994	1.50218	38.0782	42.7627	54.5666	10.3159	0.801186	10.661
0.800	3405.31	13932.6	722.035	4.83712	0.109937	1.63186	12.9682	2.04994	1.50218	40.6052	32.1355	51.8507	9.74715	0.757013	10.821
0.750	3677.66	14040.2	572.066	3.99576	0.109937	1.63186	12.9682	2.04994	1.50218	37.5421	12.3182	48.4256	9.44232	0.733338	9.5880
CO-enhanced															
1.100	3660.61	14067.0	440.693	1.94088	0.109832	1.61924	12.8129	2.02641	1.49111	19.5898	1.52120	43.2057	9.36897	0.733041	7.88827
1.050	3653.94	14255.7	464.594	1.88401	0.109832	1.61924	12.8129	2.02641	1.49111	23.1582	3.55201	46.6300	8.48705	0.664039	7.84537
1.000	3630.72	13801.7	478.038	1.95585	0.111082	1.84235	14.4681	2.08309	1.69767	28.4534	7.89617	52.0096	10.9169	0.750228	7.49216
0.950	3629.56	14320.5	514.884	1.89000	0.111082	1.84235	14.4681	2.08309	1.69767	32.3826	10.2463	51.7381	9.77730	0.671912	7.67924
0.900	3647.55	14438.4	530.320	1.87504	0.111082	1.84235	14.4681	2.08309	1.69767	36.3046	14.3795	52.6394	9.72441	0.668278	8.34448
0.870	3666.71	14364.7	528.826	1.89299	0.111082	1.84235	14.4681	2.08309	1.69767	38.0084	18.9908	52.3601	11.3945	0.783048	9.32786
0.820	3703.06	13872.5	517.824	2.05761	0.112242	2.03479	15.9193	2.21914	1.87560	42.4604	12.9375	53.7324	10.9197	0.679230	7.56001
0.800	3734.30	14190.8	520.362	2.11148	0.112242	2.03479	15.9193	2.21914	1.87560	43.4227	13.1908	54.2522	11.5639	0.719300	7.66789
0.750	3885.49	14473.8	479.532	2.64889	0.112242	2.03479	15.9193	2.21914	1.87560	43.9293	5.68844	48.4348	9.18683	0.571443	7.40766
$M_{ini} = 3\,M_\odot$, $Z_{ini} = 10^{-7}$				$\times 10^4$		$\times 10^3$	$\times 10^4$	$\times 10^5$	$\times 10^3$		$\times 10^7$		$\times 10^3$		$\times 10^3$
CNO-enhanced															
1.800	3158.40	22209.4	816.605	9.75781	0.120313	1.56544	1.14366	3.71391	1.45107	15.0468	1.73344	43.3230	7.85202	0.631304	6.8665
1.750	3122.27	21984.7	860.115	11.3645	0.120741	1.64902	1.19679	3.72209	1.52934	17.9789	2.98782	51.0273	8.71237	0.664629	7.0237
1.700	3101.29	22114.4	903.625	11.9957	0.120741	1.64902	1.19679	3.72209	1.52934	20.8686	6.34790	54.5990	9.29032	0.708717	8.2676
1.650	3065.17	22010.6	963.452	14.1761	0.121186	1.73639	1.25258	3.73027	1.61113	22.0531	7.74523	54.5884	9.84134	0.712640	7.1101
1.602	3051.19	21993.4	998.803	14.6926	0.121186	1.73639	1.25258	3.73027	1.61113	24.7114	7.84603	57.0181	9.90075	0.716942	8.1086
1.550	2999.91	22079.8	1093.98	18.9387	0.121971	1.88454	1.35087	3.76572	1.74945	27.8718	17.0124	58.8561	10.9117	0.727676	8.2811
1.500	2988.26	22088.4	1137.49	19.5126	0.121971	1.88454	1.35087	3.76572	1.74945	29.7228	18.3791	60.0656	10.4988	0.744090	8.0306
1.450	2933.49	22088.4	1251.71	26.5130	0.123218	2.11247	1.49964	3.88027	1.96251	37.5055	37.1253	66.8836	13.6682	0.812546	9.1855
1.400	2926.50	22166.2	1297.94	26.8573	0.123218	2.11247	1.49964	3.88027	1.96251	41.2179	47.1284	68.6298	12.5563	0.746443	7.9037
1.350	2924.16	22174.9	1336.01	26.5704	0.123218	2.11247	1.49964	3.88027	1.96251	44.2572	67.4315	70.6540	14.0318	0.834161	7.6342
1.304	2926.50	22131.6	1363.20	25.8818	0.123218	2.11247	1.49964	3.88027	1.96251	47.1193	43.0863	70.1846	13.2164	0.785688	8.7076
1.250	2885.71	22140.3	1482.85	33.4838	0.124894	2.40498	1.70153	3.89663	2.23483	59.8928	72.3613	77.5628	15.3208	0.799807	7.7771
1.200	2903.19	22235.4	1501.89	30.6386	0.124894	2.40498	1.70153	3.89663	2.23483	62.1005	86.2669	76.9654	14.1695	0.739701	8.2756
1.150	2931.16	22278.6	1496.45	26.7096	0.124894	2.40498	1.70153	3.89663	2.23483	66.1666	88.3011	76.1598	15.7880	0.824197	7.6751
1.100	2973.11	22295.8	1466.54	22.1032	0.124894	2.40498	1.70153	3.89663	2.23483	70.5593	109.164	73.6213	15.6457	0.816768	7.8305

Table A1 – *continued*

M	$T_{\rm eff}$	L	P	κ	He/H	C/H	O/H	N/H	$\delta_{\rm C}$	α	$\dot{M}$	v_∞	$\rho_{\rm d}/\rho_{\rm g}$	$f_{\rm C}$	$\langle a \rangle$
$M_{\rm ini} = 3\,{\rm M}_\odot, Z_{\rm ini} = 10^{-7}$				$\times 10^4$		$\times 10^3$	$\times 10^4$	$\times 10^5$	$\times 10^3$		$\times 10^7$		$\times 10^3$		$\times 10^3$
CO-enhanced															
1.150	3727.40	22182.3	609.677	1.53031	0.133332	1.31606	2.54775	206.946	1.06129	11.4187	1.41819	18.7337	4.35226	0.478442	11.0352
1.100	3735.40	22297.8	627.496	1.52378	0.133332	1.31606	2.54775	206.946	1.06129	17.1083	6.91223	26.3351	6.70094	0.736632	13.4831
1.067	3745.80	22235.9	633.235	1.53684	0.133332	1.31606	2.54775	206.946	1.06129	18.6653	12.9067	25.3804	7.07728	0.778002	13.1789
1.037	3727.00	21798.5	646.826	1.61520	0.134749	1.57958	2.75975	206.946	1.30361	28.0799	9.97957	40.7216	6.16531	0.551767	9.97913
1.000	3747.00	22198.8	662.531	1.64132	0.134749	1.57958	2.75975	206.946	1.30361	30.8209	13.3295	40.3212	6.00837	0.537722	10.8613
0.950	3792.19	22322.6	661.021	1.73928	0.134749	1.57958	2.75975	206.946	1.30361	32.6872	12.3773	39.6887	6.63601	0.593893	10.9893
0.915	3842.99	22289.5	645.315	1.89600	0.134749	1.57958	2.75975	206.946	1.30361	32.2771	12.6635	34.8753	8.34001	0.746393	10.6638
0.880	3880.59	21914.0	630.516	2.29400	0.137819	2.16406	3.24158	206.946	1.83990	50.5416	7.35495	44.2847	10.1169	0.641506	7.76959
0.850	4022.63	22343.2	576.764	2.96042	0.137819	2.16406	3.24158	206.946	1.83990	42.5482	2.71172	37.1135	8.19227	0.519465	6.83243
$M_{\rm ini} = 4\,{\rm M}_\odot, Z_{\rm ini} = 10^{-7}$				$\times 10^4$		$\times 10^4$	$\times 10^4$	$\times 10^3$	$\times 10^4$		$\times 10^7$		$\times 10^4$		$\times 10^3$
CNO-enhanced															
1.600	3038.62	25018.6	1146.48	9.15177	0.150544	6.58257	1.72841	1.79393	4.85416	3.32040	2.31899	10.1586	9.43326	0.226722	18.558
1.550	3029.66	25060.1	1188.53	9.21287	0.150544	6.58257	1.72841	1.79393	4.85416	6.92343	7.29344	20.8258	21.9100	0.526592	35.675
1.500	2927.01	24718.9	1363.40	15.4451	0.151631	8.54022	1.85720	1.79393	6.68302	11.4354	13.4321	34.4586	38.8665	0.678500	25.011
1.450	2921.31	24986.4	1423.16	15.4145	0.151631	8.54022	1.85720	1.79393	6.68302	11.9103	19.1026	33.7557	41.3796	0.722371	25.439
1.400	2922.94	25023.2	1458.57	15.1090	0.151631	8.54022	1.85720	1.79393	6.68302	12.2713	28.5085	32.6575	41.8659	0.730861	27.199
1.375	2925.38	24981.7	1471.85	14.8909	0.151631	8.54022	1.85720	1.79393	6.68302	12.6620	24.4443	32.7098	39.1021	0.682613	27.188
1.350	2859.69	24669.8	1603.88	22.2599	0.152694	10.4881	1.98536	1.79393	8.50274	17.3814	41.4701	38.8087	48.7693	0.669167	21.668
1.300	2869.14	24993.6	1648.81	21.0528	0.152694	10.4881	1.98536	1.79393	8.50274	18.4077	55.9711	39.4340	54.2351	0.744163	23.506
1.250	2887.71	25061.9	1661.21	19.4036	0.152694	10.4881	1.98536	1.79393	8.50274	21.4882	82.2577	38.3222	52.5451	0.720974	21.046
1.200	2916.39	25022.3	1646.75	17.3974	0.152694	10.4881	1.98536	1.79393	8.50274	21.2623	139.187	37.1721	53.6487	0.736117	21.873
CO-enhanced															
1.100	3790.17	25251.9	667.445	1.50060	0.159737	12.3140	2.14489	2.09668	10.1691	14.8414	1.59205	18.6041	37.9496	0.435382	10.1558
1.050	3814.74	25398.8	677.893	1.54631	0.159737	12.3140	2.14489	2.09668	10.1691	12.9893	1.45142	16.5114	21.1322	0.242442	7.52456
1.000	3823.19	24969.1	685.439	1.70630	0.161315	15.3614	2.37780	2.09695	12.9836	27.5113	4.66115	30.2699	62.1904	0.558824	9.03862
0.950	3894.23	25450.2	676.442	1.91200	0.161315	15.3614	2.37780	2.09695	12.9836	25.4080	3.40131	26.4524	48.2340	0.433416	7.83191

Table A2. Same as Table A1, but for all models except $M_{ini} = 2$, 3 and 4 $M_{\odot}$ with $Z_{ini} = 10^{-7}$ models.

M	T_{eff}	L	P	κ	He/H	C/H	O/H	N/H	δ_C	α	$\dot{M}$	v_{∞}	ρ_d/ρ_g	f_C	$\langle a \rangle$
$M_{ini} = 2\,M_{\odot}, Z_{ini} = 10^{-4}$				$\times 10^4$	$\times 10^2$	$\times 10^3$	$\times 10^4$	$\times 10^6$	$\times 10^3$		$\times 10^7$		$\times 10^3$		$\times 10^3$
CNO-enhanced															
1.250	3338.94	12916.9	522.374	5.13550	9.39632	1.56638	1.37701	3.28089	1.42868	18.1663	3.55304	49.0221	9.26062	0.756227	9.2684
1.190	3272.60	12602.6	570.602	6.21670	9.51406	1.78034	1.53969	3.50404	1.62637	22.1714	4.78770	55.8699	10.8788	0.780381	8.4654
1.150	3242.08	12965.7	621.543	6.42589	9.51406	1.78034	1.53969	3.50404	1.62637	25.2123	8.59955	57.1860	10.9897	0.788343	8.9031
1.100	3220.76	13112.8	665.690	6.53481	9.51406	1.78034	1.53969	3.50404	1.62637	27.5729	16.0594	59.0110	11.5646	0.829580	9.6414
1.070	3215.90	13091.2	681.205	6.53279	9.69428	2.10699	1.80110	4.14161	1.92688	35.0746	39.8511	64.4142	15.2790	0.925098	8.6247
1.000	3136.99	12925.0	775.883	9.36333	9.69428	2.10699	1.80110	4.14161	1.92688	39.4253	39.2466	64.3599	13.5719	0.821735	9.7659
0.950	3143.10	13158.5	813.308	8.86638	9.69428	2.10699	1.80110	4.14161	1.92688	44.2370	78.8438	65.3057	13.9913	0.847132	10.104
0.900	3179.10	13264.8	817.389	7.62180	9.69428	2.10699	1.80110	4.14161	1.92688	48.3443	51.9786	64.3025	14.0708	0.851943	8.9385
0.850	3254.64	13325.5	783.725	5.91049	9.69428	2.10699	1.80110	4.14161	1.92688	51.8245	63.4992	61.8357	14.0329	0.849648	8.7691
0.820	3322.48	13310.3	743.431	5.01595	9.69428	2.10699	1.80110	4.14161	1.92688	54.1433	49.3138	61.7336	14.1852	0.858873	12.918
0.750	3438.10	12642.1	668.964	5.56045	10.0821	2.79086	2.37194	5.75815	2.55367	73.7649	49.2142	67.6928	18.6802	0.853423	6.8885
CO-enhanced															
1.230	3403.20	12514.1	478.131	4.25313	9.50928	1.76904	1.53220	3.41822	1.61582	18.8180	1.75194	43.8845	10.0931	0.728753	7.57766
1.200	3372.04	12936.6	519.498	4.33107	9.50928	1.76904	1.53220	3.41822	1.61582	22.1539	5.21534	52.8957	10.0044	0.722342	8.70826
1.150	3344.92	13149.8	560.765	4.39201	9.50928	1.76904	1.53220	3.41822	1.61582	23.9172	5.37421	56.3700	10.0490	0.725567	8.37805
1.120	3337.66	13124.8	574.796	4.40725	9.50928	1.76904	1.53220	3.41822	1.61582	24.9763	10.2121	56.8877	12.0135	0.867411	9.77634
1.070	3270.97	12904.9	630.094	5.42814	9.66725	2.05172	1.75441	4.05309	1.87628	33.0183	15.3307	62.2296	12.4833	0.776208	8.22694
1.050	3261.07	13081.8	655.680	5.45861	9.66725	2.05172	1.75441	4.05309	1.87628	34.9095	28.4310	61.9283	13.6059	0.846014	9.37263
1.000	3254.46	13275.1	693.645	5.35957	9.66725	2.05172	1.75441	4.05309	1.87628	38.7163	24.3635	62.7492	12.3544	0.768195	9.08380
0.950	3267.01	13348.5	713.416	5.05744	9.66725	2.05172	1.75441	4.05309	1.87628	42.6281	30.3574	61.5102	12.9003	0.802139	8.92826
0.915	3290.12	13286.0	709.327	4.71961	9.66725	2.05172	1.75441	4.05309	1.87628	44.3248	31.7759	61.5741	13.1414	0.817128	8.98153
0.870	3282.86	12408.8	697.772	5.45099	9.86517	2.40456	2.04328	5.00541	2.20023	52.6909	38.6171	66.1579	16.0982	0.853604	7.88866
0.850	3303.32	12857.3	716.755	5.03197	9.86517	2.40456	2.04328	5.00541	2.20023	56.6553	59.9712	65.8274	15.6191	0.828196	7.83694
0.800	3421.51	13249.5	676.313	3.91966	9.86517	2.40456	2.04328	5.00541	2.20023	62.5362	45.6232	63.6694	15.9021	0.843203	8.09609
0.750	3628.09	13416.6	577.272	3.25685	9.86517	2.40456	2.04328	5.00541	2.20023	62.3623	28.5157	62.2468	14.4193	0.764581	7.49792
$M_{ini} = 2\,M_{\odot}, Z_{ini} = 10^{-5}$				$\times 10^4$	$\times 10^2$	$\times 10^3$	$\times 10^5$	$\times 10^5$	$\times 10^3$		$\times 10^7$		$\times 10^3$		$\times 10^3$
CNO-enhanced															
1.300	3265.46	12576.9	536.763	7.06323	9.56070	1.32209	9.95511	2.84940	1.22254	13.0549	2.71896	43.6010	8.39711	0.801335	10.676
1.240	3194.93	12274.7	589.369	8.80511	9.65633	1.50140	11.4535	2.88266	1.38687	17.3460	4.55029	50.9599	9.28072	0.780718	10.938
1.200	3155.75	12681.9	653.168	9.64457	9.65633	1.50140	11.4535	2.88266	1.38687	19.4534	5.88823	54.1910	9.50918	0.799937	10.001
1.150	3125.97	12833.0	705.774	10.40010	9.65633	1.50140	11.4535	2.88266	1.38687	21.0090	13.5384	51.3133	10.2159	0.859391	10.213
1.130	3119.70	12812.0	718.086	10.56800	9.65633	1.50140	11.4535	2.88266	1.38687	21.4855	12.6548	53.0611	9.64660	0.811497	10.422
1.090	3052.30	12312.5	770.083	15.69420	9.79182	1.76374	13.6145	2.92969	1.62760	25.5039	17.3597	57.7088	10.5748	0.758006	9.8957
1.050	3024.09	12770.0	849.425	16.94940	9.79182	1.76374	13.6145	2.92969	1.62760	29.7327	24.9733	60.8263	11.6148	0.832556	10.287
1.000	3014.68	12958.9	901.493	16.99590	9.79182	1.76374	13.6145	2.92969	1.62760	33.3294	35.2992	60.9806	11.9640	0.857583	10.642
0.950	3027.22	13047.0	926.287	15.78720	9.79182	1.76374	13.6145	2.92969	1.62760	36.3065	47.1479	60.9727	12.2716	0.879634	10.943
0.900	3064.84	13042.9	921.328	13.36980	9.79182	1.76374	13.6145	2.92969	1.62760	39.2270	64.1142	60.7041	10.9092	0.781979	11.003
0.850	2947.29	12333.5	1052.74	29.79860	10.12650	2.38802	18.8011	3.03918	2.20001	54.5560	64.8613	70.8512	16.6264	0.881700	8.2605
0.800	3064.84	12975.7	995.711	17.87920	10.12650	2.38802	18.8011	3.03918	2.20001	62.7349	64.2945	68.4908	16.7248	0.886920	8.9058
0.750	3314.34	13198.9	787.439	8.39542	10.12650	2.38802	18.8011	3.03918	2.20001	66.1491	62.5999	64.4525	16.4666	0.873227	7.6490
0.700	3990.15	13338.4	422.963	5.88501	10.12650	2.38802	18.8011	3.03918	2.20001	44.4785	1.27711	44.1531	12.8502	0.681447	5.2637

Table A2 – *continued*

M	$T_{\rm eff}$	L	P	κ	He/H	C/H	O/H	N/H	$\delta_{\rm C}$	α	$\dot{M}$	v_∞	$\rho_{\rm d}/\rho_{\rm g}$	$f_{\rm C}$	$\langle a \rangle$
$M_{\rm ini} = 2\,{\rm M}_\odot, Z_{\rm ini} = 10^{-5}$				$\times 10^4$	$\times 10^2$	$\times 10^3$	$\times 10^5$	$\times 10^5$	$\times 10^3$		$\times 10^7$		$\times 10^3$		$\times 10^3$
CO-enhanced															
1.100	3511.80	13261.9	486.157	2.61727	9.89846	1.93278	14.7245	2.97016	1.78554	27.3280	4.52347	55.9459	10.4870	0.685219	6.99248
1.050	3499.03	13420.6	516.886	2.57102	9.89846	1.93278	14.7245	2.97016	1.78554	30.2535	9.34291	55.2315	11.1952	0.731492	7.86904
1.000	3459.92	12491.0	521.076	2.97807	10.0670	2.22990	17.0100	3.03546	2.05980	36.2482	14.2681	61.6155	13.6363	0.772358	7.47469
0.950	3441.16	13363.9	588.818	2.88555	10.0670	2.22990	17.0100	3.03546	2.05980	43.6019	31.0592	60.4876	14.8818	0.842899	9.24524
0.900	3467.90	13545.3	602.785	2.70053	10.0670	2.22990	17.0100	3.03546	2.05980	48.4347	32.7648	61.7021	14.7553	0.835739	9.06443
0.850	3522.57	13619.0	595.801	2.50163	10.0670	2.22990	17.0100	3.03546	2.05980	53.3740	37.1340	59.9614	14.0226	0.794238	8.58517
0.825	3562.26	13579.4	582.532	2.43688	10.0670	2.22990	17.0100	3.03546	2.05980	53.3422	26.8432	60.3475	14.1118	0.799292	7.86681
0.750	3722.03	13256.2	518.282	2.73291	10.2899	2.60988	20.0139	3.23136	2.40974	64.8585	25.6274	62.8058	16.1179	0.780342	6.41660
$M_{\rm ini} = 2\,{\rm M}_\odot, Z_{\rm ini} = 10^{-6}$				$\times 10^4$		$\times 10^3$	$\times 10^5$	$\times 10^5$	$\times 10^3$		$\times 10^7$		$\times 10^3$		$\times 10^3$
CNO-enhanced															
1.250	3230.78	12885.9	589.111	7.24435	0.102158	1.17419	8.63692	3.23885	1.08782	13.3615	2.88796	40.9209	6.99015	0.749680	12.267
1.200	3203.10	13099.1	636.355	7.39577	0.102158	1.17419	8.63692	3.23885	1.08782	15.5386	5.52113	44.5565	7.27887	0.780645	14.110
1.150	3126.97	12538.8	689.050	10.4545	0.103290	1.38658	10.4221	3.28136	1.28236	18.9502	9.19304	52.8373	9.20854	0.837776	10.946
1.100	3083.72	13158.6	785.354	11.7567	0.103290	1.38658	10.4221	3.28136	1.28236	20.5854	15.0710	50.2585	9.06116	0.824368	11.785
1.050	3069.43	13317.3	834.414	12.0596	0.103290	1.38658	10.4221	3.28136	1.28236	23.1650	29.8243	50.8974	9.08085	0.826159	11.675
1.000	3072.11	13337.1	863.487	11.6659	0.103290	1.38658	10.4221	3.28136	1.28236	24.9805	33.9343	53.3817	9.76594	0.888488	12.494
0.950	3064.75	12345.4	841.683	13.5435	0.104249	1.57282	11.9523	3.36637	1.45330	28.3503	37.9218	57.0333	10.7191	0.860501	11.828
0.900	3080.26	13168.5	912.548	12.1504	0.104249	1.57282	11.9523	3.36637	1.45330	33.4796	38.4812	57.1488	10.6013	0.851043	11.276
0.850	3158.11	13396.6	879.841	9.09170	0.104249	1.57282	11.9523	3.36637	1.45330	37.3799	57.2383	54.6450	10.1902	0.818037	11.775
0.800	3305.18	13510.7	787.171	6.39639	0.104249	1.57282	11.9523	3.36637	1.45330	39.4929	46.2347	53.9596	10.4944	0.842462	11.018
0.750	3564.70	13555.3	619.592	4.74218	0.104249	1.57282	11.9523	3.36637	1.45330	37.2452	17.1357	48.8594	8.93152	0.716997	10.179
CO-enhanced															
1.100	3640.21	13782.6	441.560	2.02569	0.104475	1.60827	12.1786	3.29758	1.48648	19.5411	3.61445	44.0755	9.67635	0.759448	9.33071
1.050	3604.62	13616.0	469.011	2.08664	0.105664	1.81956	13.7459	3.36288	1.68210	26.6383	4.63302	50.9905	9.44236	0.654901	6.92018
1.000	3597.77	13935.7	499.833	2.02188	0.105664	1.81956	13.7459	3.36288	1.68210	28.2457	7.09100	53.1315	10.0121	0.694416	7.35582
0.950	3605.60	13962.9	515.245	1.98569	0.105664	1.81956	13.7459	3.36288	1.68210	32.4879	10.0686	52.9608	9.96443	0.691110	7.86708
0.900	3576.54	13656.8	541.733	2.14949	0.107629	2.18119	16.4232	3.42819	2.01696	44.0833	20.6530	58.5387	13.5437	0.783409	7.51190
0.850	3614.42	14058.1	557.626	2.09235	0.107629	2.18119	16.4232	3.42819	2.01696	50.6613	22.7176	58.8941	13.2656	0.767323	7.73049
0.800	3686.38	14204.4	546.067	2.14949	0.107629	2.18119	16.4232	3.42819	2.01696	24.9805	33.9343	53.3817	9.76594	0.888488	12.4940
0.750	3833.31	14248.6	497.091	2.56919	0.107629	2.18119	16.4232	3.42819	2.01696	50.2504	8.31756	55.2756	12.3380	0.713667	6.78339

Table A2 – *continued*

M	T_{eff}	L	P	κ	He/H	C/H	O/H	N/H	δ_C	α	$\dot{M}$	v_∞	ρ_d/ρ_g	f_C	$\langle a \rangle$
$M_{ini} = 2\,M_\odot, Z_{ini} = 0$				$\times 10^4$		$\times 10^3$	$\times 10^5$	$\times 10^5$	$\times 10^3$		$\times 10^7$		$\times 10^3$		$\times 10^3$
CNO-enhanced															
1.150	3339.49	14291.4	610.218	4.68494	0.120970	1.08508	7.56827	2.25733	1.00940	14.0328	6.88367	33.4370	6.39255	0.738854	12.389
1.100	3319.37	14631.5	657.922	4.66262	0.120970	1.08508	7.56827	2.25733	1.00940	17.2337	12.8259	40.2044	5.89020	0.680793	13.928
1.060	3319.37	14620.9	675.352	4.58452	0.120970	1.08508	7.56827	2.25733	1.00940	18.0478	11.4310	41.1719	5.82789	0.673591	13.414
1.000	3271.61	14509.3	737.734	5.29422	0.121855	1.25492	8.92204	2.28337	1.16570	21.5347	18.5453	46.2308	7.77300	0.777945	13.282
0.950	3294.24	14806.8	761.586	4.93485	0.121855	1.25492	8.92204	2.28337	1.16570	24.4100	19.2805	47.3174	7.70166	0.773968	12.913
0.900	3347.03	14907.8	751.495	4.45024	0.121855	1.25492	8.92204	2.28337	1.16570	25.6475	20.9610	45.7600	7.60962	0.761593	13.163
0.870	3392.28	14828.1	727.643	4.15621	0.121855	1.25492	8.92204	2.28337	1.16570	26.4785	26.4916	45.6186	8.07064	0.807734	13.305
0.820	3500.37	14158.6	649.665	3.92207	0.122519	1.35533	9.70306	2.38750	1.25830	28.2349	18.2165	44.8536	7.94338	0.736492	11.008
0.800	3573.27	14557.1	628.565	3.69338	0.122519	1.35533	9.70306	2.38750	1.25830	29.1972	15.9277	43.9736	7.19478	0.667084	11.448
0.750	3900.07	14923.7	488.206	3.75327	0.122519	1.35533	9.70306	2.38750	1.25830	19.8531	1.78389	24.2369	4.88276	0.452719	6.8978
CO-enhanced															
1.100	3718.51	15066.7	443.232	1.79454	0.122083	1.30129	9.24046	2.27491	1.20889	11.5672	1.11605	24.7375	7.14649	0.689691	11.5388
1.072	3718.03	15021.3	450.342	1.77842	0.122083	1.30129	9.24046	2.27491	1.20889	12.6125	1.49146	25.7992	5.97437	0.576572	9.91552
1.030	3697.04	14885.3	469.897	1.79859	0.122943	1.46127	10.4594	2.30974	1.35668	19.3967	2.38930	40.9011	7.95007	0.683662	9.24964
1.000	3695.35	15152.8	489.095	1.76245	0.122943	1.46127	10.4594	2.30974	1.35668	22.8812	4.50433	42.2656	7.48530	0.643695	9.09147
0.950	3703.56	15270.8	507.228	1.74662	0.122943	1.46127	10.4594	2.30974	1.35668	25.0306	7.73868	44.0875	7.76989	0.668168	9.54643
0.900	3718.75	14540.6	496.562	1.83962	0.123551	1.56243	11.1908	2.41422	1.45052	27.9964	8.94191	46.9987	8.22067	0.661195	9.03381
0.850	3751.32	15220.9	522.871	1.87171	0.123551	1.56243	11.1908	2.41422	1.45052	31.1536	9.01878	45.8575	7.83613	0.630266	8.86316
0.800	3829.09	15379.6	511.494	2.10146	0.123551	1.56243	11.1908	2.41422	1.45052	31.9521	6.18426	42.7639	8.46901	0.681169	8.66284
$M_{ini} = 3\,M_\odot, Z_{ini} = 10^{-4}$				$\times 10^4$		$\times 10^3$	$\times 10^4$	$\times 10^4$	$\times 10^4$		$\times 10^7$		$\times 10^3$		$\times 10^3$
CNO-enhanced															
2.000	3015.63	22232.3	893.878	19.3012	0.101197	1.45730	1.28232	1.52832	13.2907	12.9080	1.33334	39.9491	8.32059	0.730388	6.5853
1.950	2980.03	21988.8	944.510	23.2151	0.101736	1.55750	1.34679	1.52873	14.2282	15.8151	1.30993	49.0924	8.74770	0.717283	6.8049
1.900	2961.70	22044.1	988.392	24.5965	0.101736	1.55750	1.34679	1.52873	14.2282	16.8991	1.93883	51.7274	8.63146	0.711262	7.1828
1.850	2909.93	22038.6	1072.78	32.1942	0.102569	1.70563	1.45269	1.54045	15.6036	18.4978	2.79164	53.7915	10.5294	0.787270	6.4778
1.800	2893.75	21994.3	1116.66	34.0360	0.102569	1.70563	1.45269	1.54045	15.6036	19.6371	6.21234	56.3819	10.9576	0.825301	7.2759
1.765	2884.04	21916.9	1143.66	35.1872	0.102569	1.70563	1.45269	1.54045	15.6036	20.0889	5.50874	56.6878	10.6411	0.795623	7.3496
1.740	2840.90	21861.5	1217.93	45.5476	0.103697	1.88861	1.60004	1.54620	17.2861	22.7527	12.1768	58.3655	11.4786	0.774708	6.9923
1.700	2827.96	21889.2	1265.18	47.3895	0.103697	1.88861	1.60004	1.54620	17.2861	23.8294	14.0703	60.0060	12.7515	0.860621	7.6718
1.650	2813.94	21861.5	1312.44	49.6918	0.103697	1.88861	1.60004	1.54620	17.2861	27.1918	24.3158	62.2434	12.7081	0.857690	9.3932
1.610	2804.23	21822.8	1352.95	51.0732	0.103697	1.88861	1.60004	1.54620	17.2861	28.3828	17.3372	62.5936	11.7366	0.800490	8.4547
1.550	2753.54	21789.6	1484.59	67.8801	0.105069	2.11080	1.78883	1.55134	19.3192	35.1209	26.7236	68.8731	12.5486	0.757796	8.0252
1.500	2742.75	21817.3	1545.35	69.7220	0.105069	2.11080	1.78883	1.55134	19.3192	38.7608	44.0972	70.9562	14.4273	0.871254	8.3376
1.450	2735.20	21822.8	1602.73	70.6429	0.105069	2.11080	1.78883	1.55134	19.3192	40.4044	53.3852	71.4569	14.1214	0.852780	8.8723
1.400	2730.89	21784.1	1649.99	70.6429	0.105069	2.11080	1.78883	1.55134	19.3192	42.1429	41.2658	71.1171	13.8080	0.833854	8.6252
1.350	2693.14	21684.4	1778.26	89.5219	0.106638	2.36348	2.00525	1.55257	21.6296	50.6735	53.2345	77.4225	14.8148	0.799091	7.9518
1.300	2695.30	21800.7	1828.89	86.5289	0.106638	2.36348	2.00525	1.55257	21.6296	53.6790	129.891	78.3726	17.0171	0.917879	8.7478
1.250	2706.08	21850.5	1862.65	80.7731	0.106638	2.36348	2.00525	1.55257	21.6296	57.1269	78.5636	78.2777	16.1485	0.871027	7.9453
1.200	2725.50	21883.7	1869.40	72.9452	0.106638	2.36348	2.00525	1.55257	21.6296	60.6020	91.1719	76.7541	15.5582	0.839189	7.7713
1.150	2755.70	21889.2	1852.52	62.5848	0.106638	2.36348	2.00525	1.55257	21.6296	63.8397	91.6873	78.1608	16.2348	0.875684	8.2444
1.120	2777.27	21856.0	1825.52	56.5988	0.106638	2.36348	2.00525	1.55257	21.6296	67.0162	84.7668	77.3281	15.7920	0.851798	8.1264

Table A2 – *continued*

M	$T_{\rm eff}$	L	P	κ	He/H	C/H	O/H	N/H	$\delta_{\rm C}$	α	$\dot{M}$	v_∞	$\rho_{\rm d}/\rho_{\rm g}$	$f_{\rm C}$	$\langle a \rangle$
$M_{\rm ini} = 3\,{\rm M}_\odot, Z_{\rm ini} = 10^{-4}$				$\times 10^4$		$\times 10^3$	$\times 10^4$	$\times 10^4$	$\times 10^4$		$\times 10^7$		$\times 10^3$		$\times 10^3$
CO-enhanced															
1.250	3565.28	22295.2	680.163	2.09803	0.112988	1.01316	2.74936	1.89958	7.38224	7.28083	1.24420	16.5888	2.69006	0.425129	14.4195
1.200	3572.26	22260.3	694.587	2.06211	0.112988	1.01316	2.74936	1.89958	7.38224	9.08139	1.66900	16.7601	2.19562	0.346989	14.5219
1.150	3521.90	21873.2	742.530	2.29131	0.114533	1.28629	2.98222	1.89975	9.88068	22.4317	14.1567	39.7778	5.76723	0.680969	15.5770
1.100	3542.82	22155.4	759.829	2.22274	0.114533	1.28629	2.98222	1.89975	9.88068	24.2924	31.8863	37.8784	3.37954	0.399041	15.3359
1.050	3579.19	22208.8	758.473	2.16397	0.114533	1.28629	2.98222	1.89975	9.88068	24.5468	31.3496	37.9850	6.70059	0.791176	14.5386
1.015	3613.74	22168.8	747.957	2.13703	0.114533	1.28629	2.98222	1.89975	9.88068	25.2638	21.5587	37.0235	6.57241	0.776041	15.4065
0.980	3591.01	21826.5	774.415	2.39906	0.116819	1.70538	3.33594	1.90026	13.7179	40.3560	37.3278	45.2459	8.58464	0.730101	13.0975
0.950	3648.29	22162.1	758.133	2.35743	0.116819	1.70538	3.33594	1.90026	13.7179	40.2803	35.6810	43.6517	8.59415	0.730909	13.7282
0.900	3786.50	22308.8	690.970	2.45538	0.116819	1.70538	3.33594	1.90026	13.7179	41.3448	14.4090	40.4245	5.86793	0.499051	10.5988
$M_{\rm ini} = 3\,{\rm M}_\odot, Z_{\rm ini} = 10^{-5}$				$\times 10^4$		$\times 10^3$	$\times 10^4$	$\times 10^4$	$\times 10^4$		$\times 10^7$		$\times 10^3$		$\times 10^3$
CNO-enhanced															
1.950	3009.24	21538.1	892.832	21.0329	0.101222	1.56216	1.24712	1.00473	14.3745	14.1400	1.24103	46.1341	8.71975	0.707716	6.6426
1.900	2987.14	21668.6	939.831	22.4509	0.101222	1.56216	1.24712	1.00473	14.3745	16.6370	1.85042	52.4538	8.30533	0.674080	7.0388
1.850	2941.73	21567.1	1013.69	28.4151	0.101878	1.68577	1.33080	1.00506	15.5269	18.3658	2.11308	50.8081	10.7392	0.806927	6.1932
1.800	2923.32	21588.8	1057.33	30.1668	0.101878	1.68577	1.33080	1.00506	15.5269	19.1460	3.44584	55.3983	10.6713	0.801822	6.6586
1.750	2866.87	21574.4	1158.04	40.9473	0.102970	1.86931	1.45433	1.01967	17.2388	22.5456	6.48865	58.1546	11.7476	0.795044	6.8126
1.700	2850.91	21559.9	1208.39	43.1126	0.102970	1.86931	1.45433	1.01967	17.2388	23.7606	8.13202	60.3070	11.4520	0.775039	7.0684
1.650	2836.18	21523.6	1258.75	45.1232	0.102970	1.86931	1.45433	1.01967	17.2388	25.8751	13.8307	62.6051	11.4845	0.777234	7.8384
1.600	2782.18	21443.9	1376.25	61.6722	0.104412	2.10154	1.64560	1.03195	19.3698	32.0997	17.3409	67.1045	12.6609	0.762579	7.1745
1.550	2768.68	21501.9	1440.03	64.3015	0.104412	2.10154	1.64560	1.03195	19.3698	35.0375	24.6764	69.0913	12.5090	0.753435	8.1265
1.500	2757.64	21501.9	1493.74	66.0028	0.104412	2.10154	1.64560	1.03195	19.3698	37.3028	32.7386	70.3525	13.9301	0.839029	7.9968
1.450	2749.05	21494.6	1550.81	67.0855	0.104412	2.10154	1.64560	1.03195	19.3698	39.4166	41.1780	70.9359	13.1075	0.789482	8.6812
1.410	2745.36	21451.2	1584.38	67.3948	0.104412	2.10154	1.64560	1.03195	19.3698	41.0530	45.7026	71.6043	13.5512	0.816203	8.1277
1.380	2701.18	21291.7	1698.52	89.6664	0.106248	2.38621	1.90461	1.03311	21.9575	49.0258	46.5672	77.6232	16.1737	0.859359	7.7259
1.350	2697.50	21429.4	1748.88	89.3571	0.106248	2.38621	1.90461	1.03311	21.9575	50.8176	55.0252	77.6706	16.2000	0.860756	7.8651
1.300	2699.95	21501.9	1795.88	86.5732	0.106248	2.38621	1.90461	1.03311	21.9575	54.1770	66.7586	79.0794	16.4012	0.871443	7.9068
1.250	2708.54	21545.4	1829.45	81.6239	0.106248	2.38621	1.90461	1.03311	21.9575	59.7619	84.2515	79.0835	15.9341	0.846626	7.9505
1.200	2725.73	21559.9	1842.88	73.8907	0.106248	2.38621	1.90461	1.03311	21.9575	60.9272	121.704	79.0037	16.8505	0.895315	8.7991
1.150	2753.96	21567.1	1829.45	64.3015	0.106248	2.38621	1.90461	1.03311	21.9575	67.2020	131.499	78.4620	16.8787	0.896815	8.3430
1.125	2841.09	21538.1	1809.31	58.5790	0.106248	2.38621	1.90461	1.03311	21.9575	64.3482	74.2307	76.8827	16.2465	0.863225	7.7135
CO-enhanced															
1.150	3669.76	21933.9	639.024	1.64758	0.114683	1.28961	3.15448	19.8499	9.74162	15.3286	2.75553	25.0336	4.77237	0.571544	11.6534
1.100	3682.16	21965.3	652.737	1.64051	0.114683	1.28961	3.15448	19.8499	9.74162	17.7682	4.70819	28.8469	4.85846	0.581854	13.3947
1.056	3699.28	21896.7	658.859	1.65112	0.114683	1.28961	3.15448	19.8499	9.74162	19.7741	4.66134	28.1421	5.01614	0.600738	12.5878
1.000	3681.57	21785.3	694.857	1.79968	0.116778	1.65531	3.47668	19.8518	13.0764	34.8799	24.5790	42.4493	7.43256	0.663126	12.6145
0.950	3738.84	21956.7	686.776	1.87396	0.116778	1.65531	3.47668	19.8518	13.0764	36.4313	19.2438	41.3920	7.16523	0.639275	11.9728
0.900	3833.22	22011.0	652.492	2.08973	0.116778	1.65531	3.47668	19.8518	13.0764	37.5735	30.9386	40.7391	7.95782	0.709990	10.0633

Table A2 – *continued*

M	T_{eff}	L	P	κ	He/H	C/H	O/H	N/H	δ_C	α	$\dot{M}$	v_∞	ρ_d/ρ_g	f_C	$\langle a \rangle$
$M_{ini} = 3\,M_\odot, Z_{ini} = 10^{-6}$				$\times 10^4$		$\times 10^3$	$\times 10^4$	$\times 10^5$	$\times 10^4$		$\times 10^7$		$\times 10^3$		$\times 10^3$
CNO-enhanced															
1.900	3090.39	21640.1	826.329	14.0478	0.107099	1.53665	1.07087	5.73803	14.2956	14.0679	1.31479	43.5430	8.73270	0.712675	6.5167
1.840	3052.12	21404.2	880.362	16.7795	0.107600	1.62608	1.12975	5.74357	15.1311	16.2432	2.52741	49.1540	9.54671	0.736091	6.8871
1.800	3032.07	21557.2	922.388	17.7101	0.107600	1.62608	1.12975	5.74357	15.1311	18.4198	5.25820	51.4604	8.49704	0.655157	7.3182
1.750	2982.87	21493.5	998.435	22.7366	0.108351	1.76695	1.21963	5.78645	16.4499	20.3402	4.67849	55.5300	10.5377	0.747359	6.6427
1.700	2963.74	21544.5	1046.46	24.1113	0.108351	1.76695	1.21963	5.78645	16.4499	21.9032	8.33625	56.8996	10.2316	0.725653	7.0933
1.640	2909.06	21397.8	1142.52	32.4794	0.109424	1.95476	1.34670	5.85009	18.2009	25.6788	25.7539	61.6647	11.3057	0.724690	7.3059
1.600	2894.49	21.4935	1190.55	33.9737	0.109424	1.95476	1.34670	5.85009	18.2009	27.5721	12.3439	61.6702	11.6330	0.745668	7.1334
1.550	2881.73	21487.1	1240.58	35.4082	0.109424	1.95476	1.34670	5.85009	18.2009	30.7266	18.5587	63.2823	12.2792	0.787088	8.0537
1.510	2872.62	21423.3	1272.60	36.2450	0.109424	1.95476	1.34670	5.85009	18.2009	31.8780	26.2352	64.0918	12.3664	0.792677	8.4409
CO-enhanced															
1.200	3712.30	21914.9	593.181	1.54595	0.119582	1.229240	2.78029	197.206	9.51211	9.77604	1.02568	17.5339	3.02928	0.371543	9.72747
1.150	3716.93	21941.6	610.051	1.53126	0.119582	1.229240	2.78029	197.206	9.51211	13.6675	2.31529	25.9417	4.97348	0.610000	14.3414
1.090	3684.49	21415.9	640.079	1.62921	0.121382	1.552080	3.05415	197.206	12.4667	27.4791	30.9771	39.9155	8.89785	0.832687	10.2609
1.050	3697.01	21815.9	661.335	1.61942	0.121382	1.552080	3.05415	197.206	12.4667	29.1651	19.1169	40.7562	7.77809	0.727897	11.3047
1.000	3725.74	21903.5	668.082	1.65860	0.121382	1.552080	3.05415	197.206	12.4667	31.1523	37.0494	41.2446	7.37330	0.690016	14.1229
0.950	3772.55	21876.8	660.660	1.75655	0.121382	1.552080	3.05415	197.206	12.4667	32.8810	17.4306	38.5650	6.84473	0.640550	11.7188
0.900	3806.85	21739.7	661.672	2.07980	0.124399	2.097770	3.52555	197.206	17.4522	51.9964	17.7039	48.5809	8.88470	0.593937	8.70068
0.850	3994.43	22013.9	582.385	2.85362	0.124399	2.097770	3.52555	197.206	17.4522	49.1353	4.38012	42.9501	9.04255	0.604489	7.19564
$M_{ini} = 3\,M_\odot, Z_{ini} = 0$				$\times 10^4$		$\times 10^3$	$\times 10^4$	$\times 10^5$	$\times 10^3$		$\times 10^7$		$\times 10^3$		$\times 10^3$
CNO-enhanced															
1.705	3193.12	20915.0	769.728	9.40080	0.162251	1.83376	1.32750	4.41197	1.70101	16.0610	1.10253	43.0910	9.72756	0.667181	5.7245
1.650	3158.45	20944.1	821.882	10.4698	0.162556	1.89158	1.36560	4.42104	1.75502	16.5100	2.00024	46.2026	8.83906	0.587585	5.4973
1.600	3133.16	20766.3	858.738	11.5145	0.162828	1.94259	1.40051	4.43918	1.80254	18.8256	2.19967	50.3418	8.40362	0.543912	5.8097
1.557	3115.36	20900.5	900.462	12.0854	0.162828	1.94259	1.40051	4.43918	1.80254	21.3379	2.64154	51.3439	8.70258	0.563261	6.0833
1.500	3085.38	20911.4	960.245	13.5405	0.163100	1.99361	1.43543	4.45731	1.85007	23.9164	3.95056	54.9920	10.0183	0.614844	6.1652
1.440	3065.70	20577.6	999.120	14.7368	0.163383	2.04689	1.45924	4.47545	1.90097	26.4285	7.25363	57.8056	10.8110	0.663498	6.6509
1.400	3047.90	20958.6	1059.34	15.3826	0.163383	2.04689	1.45924	4.47545	1.90097	28.0893	14.2387	59.0958	10.4794	0.643146	7.2935
1.370	3043.22	20933.2	1077.63	15.4779	0.163383	2.04689	1.45924	4.47545	1.90097	30.0380	13.1574	58.3090	9.90343	0.607796	7.3926
1.325	3029.16	20788.1	1120.32	16.5578	0.163688	2.10585	1.51162	4.50266	1.95469	33.2075	20.4616	60.1866	11.1212	0.663778	8.3752
1.300	3024.48	20969.5	1151.57	16.6319	0.163688	2.10585	1.51162	4.50266	1.95469	35.4404	20.3661	60.5248	11.0766	0.661111	7.9328
1.252	3024.48	20984.0	1182.06	16.3037	0.163688	2.10585	1.51162	4.50266	1.95469	37.9885	29.2257	63.4203	10.1911	0.608261	8.1991
1.200	2999.27	21084.0	1265.51	18.9499	0.164645	2.28597	1.63134	4.55163	2.12284	51.7773	72.8822	69.8954	13.5973	0.747278	8.2983
1.150	3014.83	21238.9	1289.34	17.4436	0.164645	2.28597	1.63134	4.55163	2.12284	51.3141	55.9495	69.3102	13.1216	0.721137	7.9170
1.100	3044.16	21182.0	1281.16	15.3349	0.164645	2.28597	1.63134	4.55163	2.12284	54.3185	59.0855	70.0126	12.8698	0.707299	8.0798

Table A2 – *continued*

M	$T_{\rm eff}$	L	P	κ	He/H	C/H	O/H	N/H	$\delta_{\rm C}$	α	$\dot{M}$	v_∞	$\rho_{\rm d}/\rho_{\rm g}$	$f_{\rm C}$	$\langle a \rangle$
$M_{\rm ini} = 3\,{\rm M}_\odot, Z_{\rm ini} = 0$				$\times 10^4$		$\times 10^3$	$\times 10^4$	$\times 10^5$	$\times 10^4$		$\times 10^7$		$\times 10^3$		$\times 10^3$
CO-enhanced															
1.400	3582.34	21949.8	605.728	2.03051	0.167051	2.63632	1.84644	9.18902	2.45168	29.1694	4.47676	55.1713	9.75756	0.464328	5.90261
1.350	3564.13	21874.4	632.271	2.04792	0.167488	2.71915	1.90008	9.19465	2.52914	38.7477	3.81161	59.5465	12.0635	0.556476	4.87773
1.300	3558.59	21259.2	635.079	2.08050	0.167894	2.79141	1.94633	9.2409	2.59678	40.5105	4.71607	59.9084	10.9348	0.491273	4.36087
1.250	3549.09	21826.1	678.135	2.02788	0.167894	2.79141	1.94633	9.2409	2.59678	46.9114	17.4596	63.7578	14.6628	0.658764	5.07966
1.200	3543.46	21512.5	693.579	2.05043	0.168329	2.87500	2.00647	9.28716	2.67435	53.4059	15.0103	68.0937	14.4337	0.629658	5.23448
1.150	3549.09	21814.1	720.255	1.99280	0.168329	2.87500	2.00647	9.28716	2.67435	58.7739	21.7333	69.0556	14.0522	0.613019	5.28812
1.100	3567.30	21247.1	712.299	1.98027	0.168504	2.89764	2.02034	9.33341	2.69561	62.8817	31.5352	66.8338	15.1342	0.655012	6.06577
1.050	3588.68	21759.8	736.635	1.91943	0.168504	2.89764	2.02034	9.33341	2.69561	70.2173	28.4094	65.9217	13.2492	0.573430	6.06063
0.995	3636.98	20481.2	688.899	1.96022	0.168504	2.89764	2.02034	9.37967	2.69561	67.6089	26.3891	66.6502	13.6526	0.590891	5.79633
0.950	3680.53	21693.5	719.319	1.94519	0.168504	2.89764	2.02034	9.37967	2.69561	77.4801	41.0327	65.0408	13.5589	0.586833	6.19480
0.900	3763.66	21802.1	693.111	2.11308	0.168504	2.89764	2.02034	9.37967	2.69561	80.7719	57.2826	65.1831	16.7247	0.723849	5.37783
0.850	3919.57	21289.4	605.458	2.69192	0.168504	2.89764	2.02034	9.42593	2.69561	72.2165	7.49052	60.0441	12.2836	0.531639	4.84606
$M_{\rm ini} = 4\,{\rm M}_\odot, Z_{\rm ini} = 10^{-4}$				$\times 10^4$		$\times 10^4$	$\times 10^4$	$\times 10^3$	$\times 10^4$		$\times 10^7$		$\times 10^3$		$\times 10^3$
CNO-enhanced															
1.600	3021.27	26263.1	1223.82	9.03603	0.143781	6.03060	1.63390	1.62851	4.39670	4.21939	4.02808	11.6332	1.17635	0.312145	25.399
1.550	3015.89	26292.5	1261.45	9.03603	0.143781	6.03060	1.63390	1.62851	4.39670	5.90510	6.72881	17.0646	1.70121	0.451416	34.152
1.500	2934.34	26174.9	1425.25	13.5478	0.144560	7.52633	1.73001	1.62851	5.79632	11.0935	40.1708	35.7293	3.85647	0.776218	26.790
1.450	2935.24	26272.9	1465.09	13.3096	0.144560	7.52633	1.73001	1.62851	5.79632	11.4519	29.5855	31.1308	3.55209	0.714955	28.299
1.405	2940.62	26243.5	1487.22	12.9448	0.144560	7.52633	1.73001	1.62851	5.79632	11.8894	40.9672	29.4709	3.60388	0.725379	27.289
1.350	2874.30	26272.9	1666.51	19.1990	0.145623	9.47664	1.85625	1.62851	7.62039	16.4957	41.6472	37.2322	4.74226	0.726031	24.590
1.300	2892.23	26351.3	1679.79	17.8133	0.145623	9.47664	1.85625	1.62851	7.62039	18.4112	133.004	34.3871	5.16348	0.790519	24.637
1.250	2919.21	26351.3	1673.15	16.1677	0.145623	9.47664	1.85625	1.62851	7.62039	20.5669	106.194	34.2135	3.74819	0.573840	22.780
CO-enhanced															
1.150	3675.76	26520.3	757.937	1.85780	0.151401	10.3069	2.28134	1.98162	8.02556	11.6577	1.99288	17.4756	2.30061	0.334437	13.9821
1.100	3711.32	26554.5	756.304	1.84896	0.151401	10.3069	2.28134	1.98162	8.02556	15.1591	2.69638	20.8993	3.20787	0.466324	14.2606
1.050	3721.98	26505.6	772.902	1.98897	0.152675	12.8513	2.47235	1.98181	10.3790	24.0850	6.72319	29.8800	4.90957	0.551870	11.5767
1.000	3802.33	26647.6	743.244	2.05529	0.152675	12.8513	2.47235	1.98181	10.3790	21.4958	3.77084	22.3935	3.57476	0.401828	9.57462
0.972	3864.91	26579.2	713.314	2.16730	0.152675	12.8513	2.47235	1.98181	10.3790	18.5270	2.86993	19.5625	2.62650	0.295236	8.05221
$M_{\rm ini} = 4\,{\rm M}_\odot, Z_{\rm ini} = 10^{-5}$				$\times 10^4$		$\times 10^4$	$\times 10^4$	$\times 10^3$	$\times 10^4$		$\times 10^7$		$\times 10^4$		$\times 10^3$
CNO-enhanced															
1.600	3093.68	26124.4	1114.66	6.83974	0.142862	5.37275	1.52002	1.64125	3.85273	1.24775	1.30532	1.87644	4.92134	0.149026	19.300
1.550	3088.12	26054.8	1146.62	6.85780	0.142862	5.37275	1.52002	1.64125	3.85273	1.79558	2.67970	6.61737	5.17000	0.156556	20.701
1.500	2991.22	25915.7	1315.53	10.5429	0.143618	6.78398	1.61044	1.64136	5.17354	8.35267	13.6928	23.8596	24.4276	0.550859	33.056
1.450	2990.42	25972.6	1352.05	10.4165	0.143618	6.78398	1.61044	1.64136	5.17354	8.52058	12.1903	21.5878	27.0495	0.609985	32.755
1.400	2914.67	25764.1	1515.03	15.6998	0.144499	8.46971	1.71993	1.64136	6.74978	13.2999	26.8137	34.7882	40.9655	0.708069	27.571
1.350	2922.61	25980.0	1552.19	15.0336	0.144499	8.46971	1.71993	1.64136	6.74978	14.2953	38.9306	34.8483	41.7788	0.722126	28.868
1.300	2938.67	26027.0	1566.42	14.0956	0.144499	8.46971	1.71993	1.64136	6.74978	15.5810	68.1279	32.5261	42.9516	0.742397	28.512
1.272	2950.97	25966.1	1563.65	13.4819	0.144499	8.46971	1.71993	1.64136	6.74978	16.0643	78.6956	32.6764	40.2158	0.695110	29.3247

Table A2 – *continued*

M	$T_{\rm eff}$	L	P	κ	He/H	C/H	O/H	N/H	$\delta_{\rm C}$	α	$\dot{M}$	v_∞	$\rho_{\rm d}/\rho_{\rm g}$	$f_{\rm C}$	$\langle a \rangle$
$M_{\rm ini} = 4\,{\rm M}_\odot, Z_{\rm ini} = 10^{-5}$				$\times 10^4$		$\times 10^4$	$\times 10^4$	$\times 10^3$	$\times 10^4$		$\times 10^7$		$\times 10^4$		$\times 10^3$
CO-enhanced															
1.100	3785.17	26285.2	695.912	1.57039	0.150927	11.0177	2.15468	1.95640	8.86302	13.1504	1.69817	15.9886	22.5177	0.296408	10.3599
1.050	3820.36	26303.3	696.293	1.63229	0.150927	11.0177	2.15468	1.95640	8.86302	12.2253	1.71194	14.7973	25.3087	0.333146	9.88877
1.000	3837.96	26310.6	709.626	1.83125	0.152537	14.2860	2.40283	1.95654	11.8832	24.6081	4.09965	27.2018	49.5283	0.486260	8.87579
0.950	3940.20	26444.8	670.771	2.13465	0.152537	14.2860	2.40283	1.95654	11.8832	22.7546	2.26200	21.4764	31.8215	0.312417	7.05192
$M_{\rm ini} = 4\,{\rm M}_\odot, Z_{\rm ini} = 10^{-6}$				$\times 10^4$		$\times 10^4$	$\times 10^4$	$\times 10^3$	$\times 10^4$		$\times 10^7$		$\times 10^4$		$\times 10^3$
CNO-enhanced															
1.600	3056.28	25099.8	1123.72	8.22070	0.142591	6.00088	1.62127	1.76576	4.37961	1.75155	1.78657	5.65076	5.42277	0.144455	16.220
1.550	3048.34	25065.2	1160.62	8.26799	0.142591	6.00088	1.62127	1.76576	4.37961	2.95001	3.10306	9.93794	8.93528	0.238023	22.341
1.500	2955.41	24869.2	1324.78	12.8547	0.143407	7.48672	1.72073	1.76576	5.76599	10.2694	11.6918	29.8459	31.3296	0.633909	29.344
1.450	2951.44	24973.0	1369.05	12.8075	0.143407	7.48672	1.72073	1.76576	5.76599	10.9875	1.91926	32.6459	32.4373	0.656324	29.304
1.407	2953.02	24938.4	1394.87	12.5710	0.143407	7.48672	1.72073	1.76576	5.76599	11.4217	21.8926	32.8370	36.3615	0.735725	28.996
1.350	2884.39	24920.7	1568.48	18.5363	0.144385	9.25377	1.83611	1.76576	7.41766	15.1808	44.8265	37.5033	46.8478	0.736833	25.805
1.300	2895.89	25012.3	1594.29	17.5425	0.144385	9.25377	1.83611	1.76576	7.41766	16.0896	66.8600	36.3088	47.7197	0.750547	26.304
1.250	2915.58	25029.5	1600.36	16.1603	0.144385	9.25377	1.83611	1.76576	7.41766	17.9144	82.3470	33.9071	50.0389	0.787024	26.256
CO-enhanced															
1.090	3775.79	24994.8	674.877	1.54866	0.152228	13.0274	2.2125	2.05395	10.8149	17.7968	2.88524	23.7196	50.2826	0.542428	10.3451
1.050	3797.12	25354.7	688.286	1.58295	0.152228	13.0274	2.2125	2.05395	10.8149	18.1129	2.87756	22.1834	36.5738	0.394543	9.18635
1.000	3841.09	25413.5	685.238	1.68090	0.152228	13.0274	2.2125	2.05395	10.8149	18.2486	2.86271	20.9475	30.8867	0.333193	8.35958
0.950	3871.56	25318.0	687.676	1.98455	0.154504	17.5785	2.5712	2.05449	15.0073	40.8401	6.83862	39.7812	55.7683	0.433542	8.26986
0.900	4037.32	25549.4	616.976	2.67512	0.154504	17.5785	2.5712	2.05449	15.0073	24.3846	1.47272	24.3480	55.3056	0.429946	5.73953
$M_{\rm ini} = 4\,{\rm M}_\odot, Z_{\rm ini} = 0$				$\times 10^4$		$\times 10^4$	$\times 10^4$	$\times 10^3$	$\times 10^4$		$\times 10^7$		$\times 10^3$		$\times 10^2$
CNO-enhanced															
1.550	3004.09	24654.4	1206.50	10.9489	0.191974	7.31515	1.98422	2.35083	5.33093	3.94484	2.09875	11.6642	1.26130	0.276033	1.9355
1.500	2934.46	24635.1	1347.82	15.1860	0.192583	8.60712	2.07809	2.36755	6.52903	10.1968	11.8647	34.4380	2.66649	0.476473	2.7915
1.450	2928.71	24731.0	1396.54	15.2088	0.192583	8.60712	2.07809	2.36755	6.52903	10.7991	17.2217	37.2506	3.10405	0.554661	3.0968
1.400	2898.26	24588.8	1482.08	17.8334	0.192984	9.40438	2.13842	2.36755	7.26596	11.8515	15.2341	35.6180	3.80695	0.611268	2.4041
1.350	2900.30	24734.9	1526.72	17.3887	0.192984	9.40438	2.13842	2.36755	7.26596	12.2301	15.7419	32.5745	3.85461	0.618919	2.3183
1.300	2867.66	24418.4	1617.01	21.3985	0.193604	10.6662	2.23583	2.36755	8.43037	14.3101	23.2360	35.9948	4.30871	0.596276	2.1278
1.250	2879.90	24763.3	1658.61	20.0718	0.193604	10.6662	2.23583	2.36755	8.43037	15.6117	43.5326	35.9164	4.72500	0.653886	2.1286
1.200	2902.34	24799.9	1662.66	18.3691	0.193604	10.6662	2.23583	2.36755	8.43037	18.3262	58.1988	36.1284	4.79241	0.663214	2.2690

Table A2 – *continued*

M	$T_{\rm eff}$	L	P	κ	He/H	C/H	O/H	N/H	$\delta_{\rm C}$	α	$\dot{M}$	v_∞	$\rho_{\rm d}/\rho_{\rm g}$	$f_{\rm C}$	$\langle a \rangle$
$M_{\rm ini} = 5\,{\rm M}_\odot, Z_{\rm ini} = 10^{-4}$				$\times 10^4$		$\times 10^4$	$\times 10^4$	$\times 10^3$	$\times 10^4$		$\times 10^7$		$\times 10^4$		$\times 10^2$
CNO-enhanced															
1.450	3156.83	31888.7	1338.92	5.06238	0.165217	5.78915	2.42856	1.73913	3.36059	1.58642	4.09535	5.31577	3.71425	0.128944	2.4288
1.400	3100.55	31820.7	1465.27	6.71101	0.165788	6.98985	2.50124	1.73913	4.48861	7.63765	19.3213	19.1998	18.7954	0.488523	3.6688
1.350	3126.53	31937.4	1462.93	6.31041	0.165788	6.98985	2.50124	1.73913	4.48861	8.14753	20.0081	15.9822	16.2788	0.423115	3.2800
1.330	3137.71	31888.7	1458.25	6.17174	0.165788	6.98985	2.50124	1.73913	4.48861	8.12276	21.9824	14.6053	14.1822	0.368621	3.0160
CO-enhanced															
1.100	3870.29	32226.1	774.846	1.91793	0.169942	10.7233	2.84210	1.88837	7.88120	10.7892	1.31327	12.3453	15.7767	0.233545	0.9440
$M_{\rm ini} = 5\,{\rm M}_\odot, Z_{\rm ini} = 10^{-5}$				$\times 10^4$		$\times 10^4$	$\times 10^4$	$\times 10^3$	$\times 10^4$		$\times 10^7$		$\times 10^4$		$\times 10^2$
CNO-enhanced															
1.450	3189.53	30675.0	1239.85	4.53491	0.166764	5.68728	2.41216	1.83212	3.27512	1.06547	1.25136	1.54306	3.80944	0.135700	2.3862
1.400	3115.15	30664.3	1389.61	6.23243	0.167337	6.93248	2.49292	1.83221	4.43956	8.44758	19.9802	22.3217	21.8578	0.574398	4.3401
1.350	3136.66	30664.3	1391.63	5.89292	0.167337	6.93248	2.49292	1.83221	4.43956	8.30818	22.7109	20.8376	20.7950	0.546470	4.2711
1.300	3096.33	30707.3	1502.94	7.59044	0.168007	8.20920	2.56376	1.83230	5.64544	12.7565	50.7684	24.7468	25.9658	0.536599	3.2370
1.250	3138.45	30739.5	1472.58	6.85485	0.168007	8.20920	2.56376	1.83230	5.64544	13.8330	48.4231	24.5847	25.9371	0.536008	3.4423
$M_{\rm ini} = 5\,{\rm M}_\odot, Z_{\rm ini} = 10^{-6}$				$\times 10^4$		$\times 10^4$	$\times 10^4$	$\times 10^3$	$\times 10^4$		$\times 10^7$		$\times 10^4$		$\times 10^2$
CNO-enhanced															
1.450	3142.78	30215.0	1294.98	5.36104	0.163058	6.11749	2.27678	1.78645	3.84071	2.11325	4.72581	7.09111	4.76467	0.144733	2.2432
1.417	3150.60	30190.3	1301.72	5.24999	0.163058	6.11749	2.27678	1.78645	3.84071	2.42082	5.82691	7.44480	5.26745	0.160006	2.4163
CO-enhanced															
1.050	3917.13	30586.5	728.383	1.84213	0.170688	13.8482	2.88997	1.96628	10.9582	10.7141	1.50135	15.5986	15.9509	0.169821	0.5885

This paper has been typeset from a TEX/LATEX file prepared by the author.